MULTI-MODAL OPTICAL NEUROIMAGING AND APPLICATIONS

By

Hang Yu

A thesis submitted to Johns Hopkins University in conformity with the requirements for the degree of Master of Science in Engineering

Baltimore, Maryland

August 2015

Abstract

Optical imaging tools provide superior details than MRI, PET in monitoring the physiological and pathological state of brain in preclinical models. By combining different optical imaging modalities, a variety of physiological parameters (e.g. cerebral hemodynamics, metabolism and neuronal activity) could be detected simultaneously; such simultaneous imaging is expected to profoundly enhance our understanding of normal brain regulation and its disruption from neurovascular disorders.

As a part of this thesis, I designed a multi-modal optical imaging system that could perform simultaneous laser speckle contrast imaging, wide-field fluorescence imaging and optical intrinsic signal imaging. The principles, processing methods and applications of these imaging modalities are presented in Chapter 1. The system was first applied to study a new atherothrombotic stroke model and to evaluate the recovery of stroke from different treatment protocols in mice (Chapter 2). Cerebral blood flow changes and thrombus formations were imaged by laser speckle contrast imaging and wide-field fluorescence imaging, respectively. We concluded that the combination treatment of tissue plasminogen activator and cathepsin G inhibitor improved the neurological outcomes of ischemic brain injury from induced atherothrombotic stroke.

To investigate brain activity in high-resolution by optical imaging tools, cranial window preparation is an essential procedure to allow optical access to the brain. We also employed the optical imaging system to investigate the effects of cranial windows on monitoring neurovasculature by laser speckle contrast imaging (Chapter 3). Open-skull and thin-skull cranial window procedures were performed in separate experiments, and the neurovasculature underlying the cranial windows were monitored for fourteen days.

The differences between two window types were systematically compared by parameters such as contrast-to-noise ratio and microvessel density.

Finally, the last part of my thesis was to miniaturize the multi-modal bench-top imaging system to a head-mounted microscope, which allows imaging on awake freely moving animals. The natural physiological state of brain activities can be detected without the confounding effects of anesthetics. The current version of the microscope weighs less than 5 g and is able to perform laser speckle contrast imaging, wide-field fluorescence imaging and optical intrinsic signal imaging simultaneously. We are currently testing the miniaturized microscope to study a brain tumor murine model. Finally, I describe the current progress of miniaturized optical neuroimaging systems on awake moving animals in Chapter 4 of this thesis.

Thesis reviewers: Dr. Arvind Pathak, Dr. Nauder Faraday, Dr. Nitish Thakor.

Thesis Committee

Arvind P. Pathak, Ph.D.

The Russel H. Morgan Department of Radiology & Radiological Science

Johns Hopkins University

Nauder Faraday, M.D, MPH

Department of Anesthesiology & Critical Care Medicine

Johns Hopkins University

Nitish V. Thakor, Ph.D.

Department of Biomedical Engineering

Johns Hopkins University

Acknowledgements

First and foremost, I would like to express my gratitude to primary supervisors Dr. Arvind Pathak and Dr. Nitish Thakor for providing me the opportunity to conduct research on these challenging yet fruitful projects. This work would not have been possible without their kindly mentoring and support.

I thank Dr. Nauder Faraday and Dr. Kathryn Schunke for letting me to be a part of the atherothrombotic stroke project. I also thank Prof. Betty Tyler from Neurosurgery for the guidance and support on animal surgery.

This thesis would have not been possible without the support from my colleagues and friends in the Neuroengineering and Biomedical Instrumentation Laboratory. I am grateful to have shared a part of my life with you.

Finally, very special thanks to my family and friends (Ruoxian Deng, Janaka Senarathna, Dr. Tharindu De Silva) for their continued support and confidence in me.

Table of Content

List of Figures

List of Tables

CHAPTER 1 INTRODUCTION AND BACKGROUND

This chapter gives a brief introduction to the optical imaging modalities employed in this thesis, namely laser speckle contrast imaging (LSCI) and optical intrinsic signal imaging (OISI). The imaging principles, characteristics and processing methods of these two imaging modalities are covered, followed by their use in pre-clinical studies. These applications include neurophysiological monitoring in healthy rodents as well as neurovascular disorders such as ischemic stroke and glioma models.

1.1 Laser speckle contrast imaging (LSCI)

1.1.1 Characteristics of LSCI

Laser speckle contrast imaging (LSCI) is a two-dimensional, wide-field optical imaging technique that has been used to investigate vasculature (Murari, Li et al. 2007) and associated blood flow (Briers and Fercher 1982) in both clinical (Tamaki, Araie et al. 1997, Bray, Forrester et al. 2006, Richards, Towle et al. 2014) and pre-clinical studies (Jones, Shin et al. 2008, Li, Downey et al. 2011, Schrandt, Kazmi et al. 2015).

Unlike two-photon laser scanning microscopy, LSCI is a wide-field imaging technique that does not require scanning of a laser beam to form an image. This endows LSCI with a temporal resolution (~ second) that is capable of capturing relatively fast physiological changes (e.g. changes in blood flow). LSCI can also provide more spatial information than the standard method for *in vivo* blood flow measurement, laser Doppler flowmetry (LDF) (Boas and Dunn 2010). Unlike the fiber optic probe in LDF that only provides relative flow changes in a single spatial location, a high-resolution 2D distribution or ‘map’ of blood flow can be obtained using LSCI. Also, the contrast in LSCI originates from flowing red blood cells inside vessels. No endogenous fluorescence dye is needed, thereby eliminating phototoxicity and the complications associated with extrinsic contrast injections. Also, the intrinsic contrast allows an extended monitoring of the sample or tissue being studied. Researchers can monitor the same subject for days, weeks or months (Holtmaat, Bonhoeffer et al. 2009). Owing to the simplicity of imaging setup, LSCI can be easily combined with other imaging modalities or electrophysiological recordings.

However, LSCI also has its limitations. All the vessels resolved by LSCI are compressed into a 2D image. The depth-integrated image can make it difficult to interpret the images in applications where depth resolution is important. Besides, only a relative blood flow change can be measured by LSCI, the absolute value of flow velocity cannot be measured.

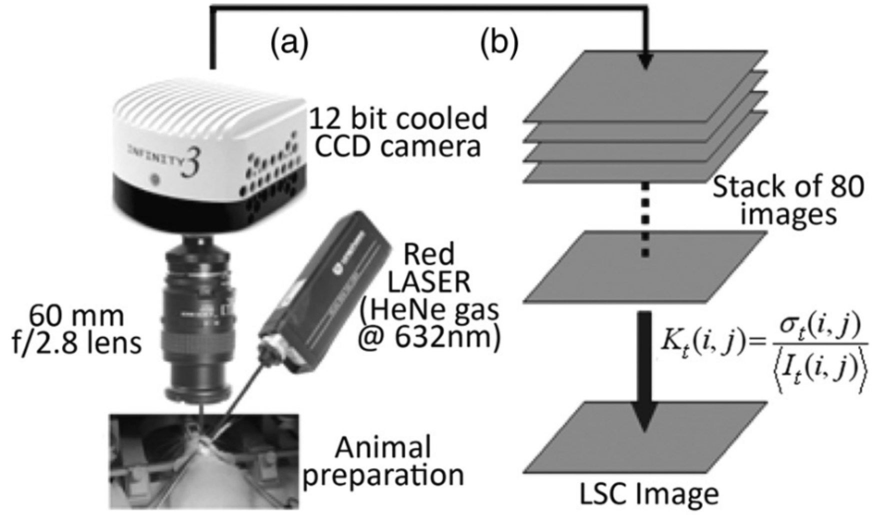

Figure 1.1: Schematic of laser speckle contrast imaging system and a typical processing scheme.

(a) System showing major components of a laser speckle contrast imaging system. (b) Temporal processing algorithm for processing laser speckle contrast image, a stack of 80 raw images was used in this case. Image adapted from (Rege, Seifert et al. 2012).

1.1.2 LSCI system

A typical laser speckle contrast imaging system setup is shown in Fig 1.1(a). A laser source is first expanded by a beam expander and employed for illumination. A neutral density (ND) filter set is optional for adjusting the laser intensity for different sample types. Laser wavelengths in the range from 600 to 900 nm are generally used, and a higher tissue penetration depth can be achieved by using a longer wavelength laser. A digital CCD camera is then used to collect the back-scattered light from the sample via a focusing optical system. Practically, a camera with a frame rate greater than 10 frames per second (fps) is desirable. A macro lens or microscope objective lens is selected for the focusing optics. An additional white light source is usually incorporated for initial focusing of the lens, since the speckles created by the laser illumination make it difficult to judge the degree of focus. According to previous publication (Dunn, Bolay et al. 2001), an imaging depth of 500 to 1000 μm can be achieved by LSCI system in brain imaging of rodents. The imaging depth of a particular system is largely determined by the laser wavelength and the focusing optics.

Because of the simplicity of LSCI imaging setup, LSCI can be easily combined with other imaging modalities and/or electrophysiological monitoring systems. Multiple physiological parameters can be obtained simultaneously through the multi-modality imaging system. The relationship between different biological parameters can then be studied, which may lead to new discoveries and improve the credibility of single parameter experiments. In (Jones, Shin et al. 2008), LSCI was combined with multispectral reflectance imaging (MSRI) in the study of focal cerebral ischemia. Cerebral metabolic rate of oxygen ($CMRO_2$), a key factor in studying brain metabolic functions, was obtained by combining these two imaging modalities. LSCI was coupled with voltage-sensitive dye (VSD) imaging in investigating cortical spreading depression in (Obrenovitch, Chen et al. 2009). Local cellular depolarization from cortical spreading depression (from VSD) and CBF changes (from LSCI) were recorded simultaneously with high spatial and temporal resolution, revealing the relationship between the spreading depression and associated CBF changes.

Recently, LSCI has also been integrated with a surgical microscope for intraoperative monitoring of CBF (Richards, Towle et al. 2014). This new microscope was applied to ten patients undergoing brain tumor resections and demonstrated an improved visualization of CBF changes during neurosurgical procedures.

1.1.3 LSCI processing schemes

Under coherent light illumination, the scattered photons from the specimen generate a speckle pattern on the camera. Moving scatter particles, e.g. red blood cells (RBCs) within vessels, blur this speckle pattern. The degree of blurring is defined as the speckle contrast *K* and is given by:

$$K(x,y) = \frac{\sigma_n}{\mu_n} \tag{1}$$

where σ_n and μ_n stand for the standard deviation and mean of the pixel values in a defined neighborhood 'n' (Senarathna, Rege et al. 2012). Speckle contrast *K* ranges from 0 to 1. Because of the blurring effect, vessels with patent blood flow exhibit a lower speckle contrast *K* than the background. A higher flow velocity would result in a higher degree of blurring and thus in lower speckle contrast *K* values. Vessels appear as grey in LSCI images (speckle contrast *K* maps), and darker vessels indicate a higher flow velocity.

Even though the flow velocity is inversely proportional to speckle contrast *K*, the exact relationship between flow velocity and speckle contrast *K* is complicated. Based on the physical model of LSCI, the relationship can be described by **Eq. 2** (Briers and Webster 1996) (Boas and Dunn 2010) under certain assumptions:

$$K = \left\{ \left[\frac{\tau_c}{T} + \frac{\tau_c^2}{2T^2} \right] \left(e^{-2T/\tau_c} - 1 \right) \right\}^{1/2} \quad (2)$$

Here, *T* is the camera exposure time, and τ_c is the speckle correlation time (τ_c is considered to be inverse proportional to flow velocity). Although absolute flow velocity cannot be obtained from LSCI, being able to quantify or assess relative CBF changes is sufficient for most applications. The nonlinear relationship between *K* and $1/\tau_c$ (inverse correlation time) makes it time-consuming to infer the real value of $1/\tau_c$ from *K* by non-linear curve fitting. Thus, $1/K^2$ is usually considered to be a good estimate of $1/\tau_c$. **Fig. 1.2(a)** shows an example of normalized blood flow map using the $1/K^2$ approximation.

The spatial and temporal resolution of LSCI images can be adjusted by choosing different processing schemes. The averaging neighborhood 'n' in equation 1 can be selected either in spatial (Fercher and Briers 1981), temporal (Cheng, Luo et al. 2003) or spatiotemporal (Duncan and Kirkpatrick 2008) (Cheng and Duong 2007) domain across the raw image stack. **Fig. 1.2(b)** shows a representative image with temporal processing scheme (Cheng, Luo et al. 2003).

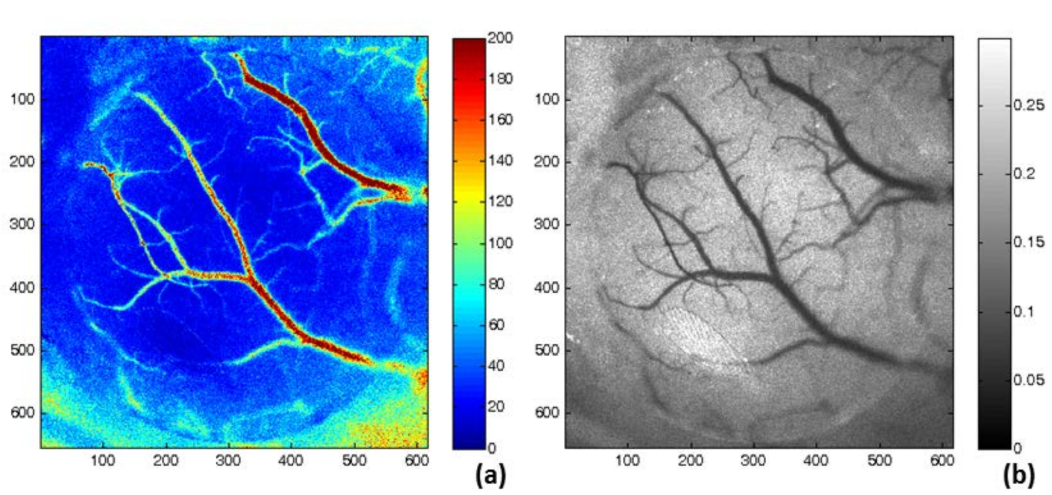

Fig. 1.2: Examples of flow maps and k maps for LSCI image

(a) Relative cerebral blood flow (CBF) distribution using the *1/K*^{2} approximation and (b) LSCI image using the temporal processing scheme in a healthy mouse brain.

1.1.4 Key determinants of LSCI performance

The quality of LSCI image contrast depends on several factors, such as the speckle size, camera exposure time and the extent of the spatial neighborhood used for averaging. These factors need to be carefully adjusted for different experimental conditions.

1.1.4.1 Speckle size

Speckle size can be described by the following equation:

$$D_{speckle} = 2.44\,\lambda(1+M)f_{\#} \tag{3}$$

In (3), $D_{speckle}$ is the diameter of the speckle Airy disk, λ is the wavelength of the laser used for illumination, M is the magnification of the lens system and $f_{\#}$ is the f number of the lens system (ratio of the lens' focal length to the diameter of entrance pupil). (Kirkpatrick, Duncan et al. 2008) reported that the sampling rate must be at or above the Nyquist criteria in order to maximize the speckle contrast of LSCI, which means that the speckle size $D_{speckle}$ must be larger than twice the size of detector pixels. However, the spatial resolution would decrease if too large a speckle size were used. Therefore, a speckle size that is twice the size of a detector pixel is considered optimal.

1.1.4.2 Camera exposure time

Using too low an exposure time (< 1 ms) will result in speckle contrast approaching 1, since the blurring of speckle contrast is small at low exposure time. Also, enough photons may not be collected by the camera at low exposure times, which causes a decrease in signal to noise ratio. Conversely, using too large an exposure time (> 50 ms) will result in speckle contrast approaching 0, eliminating the contrast between blood vessels and background tissue. Therefore, camera exposure time needs to be tuned to maximize the sensitivity of speckle contrast to blood flow.

If the purpose is to resolve all possible vascular structures in the sample, the sensitivity of LSCI to absolute flow changes S_a needs to be optimized. The sensitivity S_a for measuring absolute flow changes is defined by (Yuan, Devor et al. 2005),

$$S_a = \left|\frac{dK}{dv}\right| \tag{4}$$

Here, K is the speckle contrast and v is the blood flow velocity. As shown in **Fig 1.3 (a)**, absolute sensitivity S_a reaches its maximum value when the exposure time is of the order of the autocorrelation time τ. Vessels of smaller diameter tend to have lower blood flow velocities and hence larger autocorrelation time τ_c. Thus, a longer exposure time is needed to resolve micro-vessels (White, George et al. 2011).

On the other hand, if the purpose of the experiment is to measure cerebral blood flow (CBF) changes, the sensitivity of LSCI to relative CBF change ($^{\Delta v}/_{v}$) needs to be considered. The sensitivity of LSCI to relative CBF changes S_r can be defined by,

$$S_r = \left| \frac{\frac{dK}{K}}{\frac{dv}{v}} \right| \tag{5}$$

As shown in **Fig 1.3(b)**, the trend for S_r is quite different compared to S_a. When the exposure time T < 1.8τ_c, S_r increases along with the exposure time. When T > 1.8τ_c, S_r remains at a maximum of ~ 0.5. However, (Yuan, Devor et al. 2005) reported that the speckle contrast noise also increases with exposure time. As shown in **Fig 1.3(c)**, contrast-to-noise ratio (CNR) reached its peak at an exposure time of ~ 5 ms (More information on contrast-to-noise ratio can be found in Chapter 3). Thus, exposure time should be optimized as a trade-off between relative sensitivity S_r and speckle contrast noise. **Fig1.2 (d)** illustrates the effect of exposure time on the quality of LSCI images. As the camera exposure time increases, more small vessels could be visualized. But at the same time, an increase in speckle contrast noise is visible.

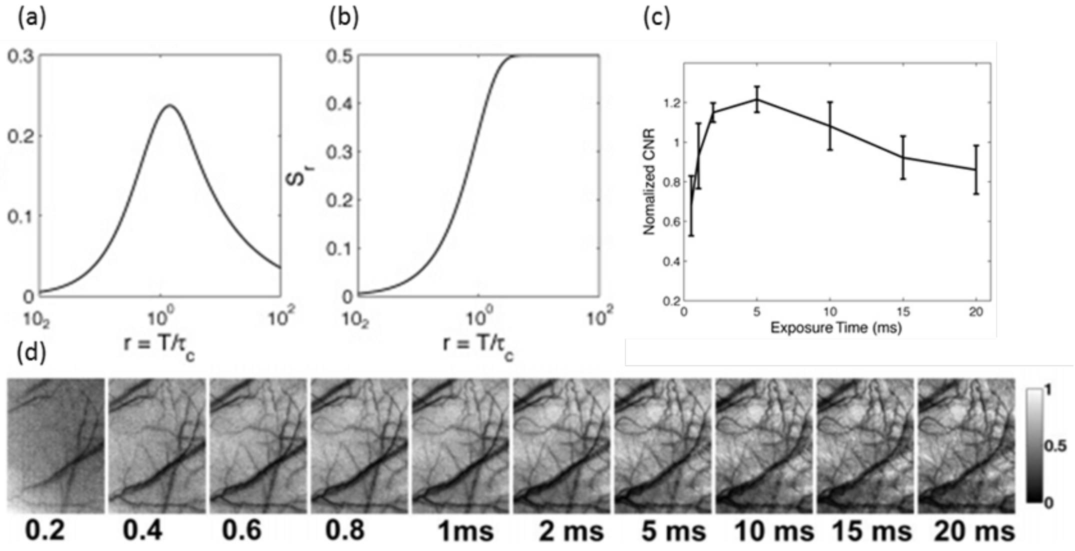

Figure 1.3 Effects of camera exposure time on laser speckle contrast.

(a) The relationship between absolute sensitivity S_a and camera exposure time. (b) The relationship between relative sensitivity S_r and camera exposure time. (c) LSCI images of the same region of rat cortex acquired with different camera exposure times. Image adapted from (Yuan, Devor et al. 2005) and (Senarathna, Rege et al. 2012).

1.1.1.1 Spatial extent of the neighborhood used for averaging

A large averaging neighborhood will limit the resolution in the domain (spatial, temporal or spatiotemporal) in which the averaging is conducted. Choosing a small neighborhood will result in an inaccurate statistical estimation of local speckle contrast. Practically, either a 5 × 5 or 7 × 7 neighborhood is used to calculate speckle contrast *K* in the spatial domain. A stack of 40 or 80 raw LSCI images is used to calculate speckle contrast *K* in temporal domain.

1.1.5 LSCI applications

LSCI is able to obtain microvascular morphology and cerebral blood flow (CBF) data with a high temporal (~ 1s) and spatial ($\sim 10\ \mu m$) resolution over a large field of view (5 mm × 5 mm), making this imaging modality suitable for studying brain function in a variety of applications. (Li, Jia et al. 2009) employed LSCI to study the neurovascular response to electrical stimulation of rat peripheral trigeminal nerve. (Dunn, Bolay et al. 2001) utilized LSCI to investigate CBF dynamics during focal cerebral ischemia and cortical spread depression. (Dufour, Atchia et al. 2013) demonstrated that LSCI could be an intrinsic method to monitor blood brain barrier integrity. LSCI was also used to evaluate the recovery of nerve injury after optogenetic stimulation (Li, Downey et al. 2011). Since no endogenous contrast agent is needed, LSCI is an ideal tool for longitudinal, chronic studies. (Rege, Seifert et al. 2012) elegantly demonstrated this by monitoring angiogenesis in a rat glioma model.

1.2 Optical intrinsic signal imaging (OISI)

Optical Intrinsic Signal Imaging (OISI) exploits the unique absorption spectra of oxy- and deoxy-hemoglobin (HbO_2 and HbR) to investigate hemodynamics in brain. Oxygen is delivered to tissue by converting HbO_2 to HbR, so the changes in oxygenation are reflected by the relative concentration changes of HbO_2 and HbR, respectively.

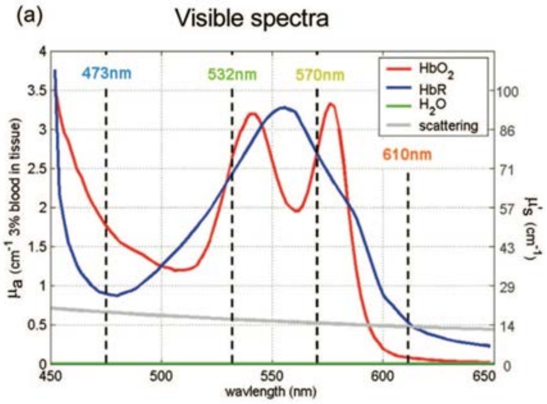

Figure 1.4 Absorption spectra of HbO_2, HbR and water in the visible light range

Image adapted from (Hillman 2007).

1.2.1 Visualize functional activation by OISI

Hemoglobin is a major absorber in the visible and near-infrared wavelengths in the brain (**Fig 1.4**). By illuminating the exposed cortex sequentially with multiple wavelengths, and capturing the reflectance images through a camera, the oxygenation state can be obtained. If the absorption coefficients of HbO_2 and HbR are the same for a certain wavelength (the “isosbestic” point, e.g. ~ 530, 797 nm), the change in total hemoglobin concentration (HbT) can also be measured. The modified Beer-Lambert law is then used to calculate the concentration changes in HbO_2 and HbR from the measured changes in image intensity as follows:

$$\ln\left[\frac{I(t)}{I(t_0)}\right]_{\lambda} = -\left(\varepsilon_{HbO_2}(\lambda)\Delta C_{HbO_2} + \varepsilon_{HbR}(\lambda)\Delta C_{HbR}\right)D(\lambda) \tag{3}$$

$\ln\left[{I(t)}/{I(t_0)}\right]$ is the change in image intensity between t and t_0 , ε is the molar extinction coefficient at a specific wavelength λ, ΔC is the change in concentration for HbO_2 and HbR, and D is the differential pathlength factor which accounts for the wavelength-dependent tissue scattering effect. The differential pathlength factor can be estimated using Monte Carlo simulations of light propagation (Wang, Jacques et al. 1995). Failure to correctly estimate the differential pathlength factor will result in incorrect calculation of HbO_2 and HbR concentration changes. If more than two wavelengths are available, HbO_2 and HbR can be calculated using a linear model (Hillman 2007).

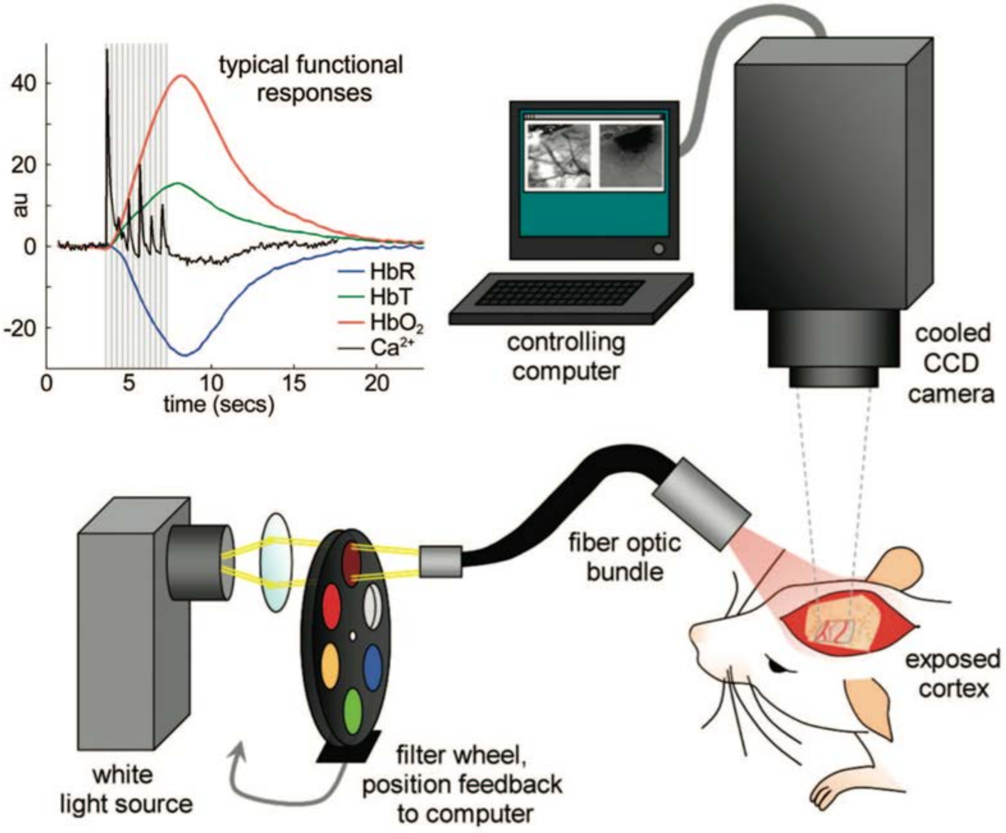

Figure 1.5 Set up of optical intrinsic signal imaging system and typical functional response from HbO_2, HbR, HbT and Calcium imaging

Image adapted from (Hillman 2007).

1.2.2 Hemoglobin saturation by OISI

The previous method is often used to measure hemodynamic changes from functional activation, wherein the concentration change in HbO_2, HbR and HbT across a time interval can be obtained. If no perturbation is present and the spatial distribution of oxygenation is a more important parameter, hemoglobin saturation (HbSat) map can be calculated from the same dataset using the following model:

$$\ln\left(\frac{I}{I_0}\right) = \left(\varepsilon_{HbO_2}(\lambda)C_{HbO_2} + \varepsilon_{HbR}(\lambda)C_{HbR}\right)L + SL \tag{4}$$

Derived from modified Beer-Lambert law, I is the pixel intensity from the reflectance image, and I_0 is the reference light selected from avascular region in the same image. ε is the molar extinction coefficient at a specific wavelength λ, C is the concentration of HbO_2 and HbR, L is the pathlength factor and S is the pathlength-dependent scattering coefficient.

A linear least-squares regression model is often used to calculate the hemoglobin saturation. The calculated HbSat value of each pixel is accepted or rejected based on R^2 values, which is used to describe the degree of fit between the data and model. R^2 is calculated from the standard definition for the coefficient of determination, $R^2 = 1 - SS_e/S_t$, where SS_e is the error of sum and S_t is the total variance. Pixel values with $R^2 < 0.9$ were rejected in a previous study (Sorg, Hardee et al. 2008). Tumor hypoxia development in dorsal window chamber model was detected using HbSat maps in (Sorg, Moeller et al. 2005).

CHAPTER 2 IN VIVO MULTI-MODAL IMAGING OF AN ATHEROTHROMBOTIC STROKE MODEL

2.1 Introduction

Stroke is the second leading cause of death in the US and the third leading cause of death worldwide (Murray and Lopez 2013). According to the statistical report from American Heart Association (Mozaffarian, Benjamin et al. 2015), 87% of strokes in the US are ischemic in nature. There are two main types of ischemic stroke: atherothrombotic stroke and cardioembolic stroke, which differ in the location of the initial blood clots. Atherothrombotic stroke accounts for ~80 % of the ischemic strokes in the US. This subclass of ischemic stroke occurs when a blood clot forms on an atherosclerotic plaque within a large extra- or intracranial artery (usually the carotid, aorta or cerebral artery is the main source of occlusion) (Davi and Patrono 2007). The disrupted plaque is unstable and embolizes distally, which activates platelets and produces thrombi, occluding major cerebral vessels and distal micro-vessels (**Fig 2.1**). Since many patients possess overlapping or indeterminate syndromes when experiencing a stroke, it is difficult to accurately classify clinical stroke events. However, data from epidemiologic studies and research on anti-platelet therapies have shown that atherothrombosis is a common cause of ischemic stroke in humans (Petty, Brown et al. 1999, Warden, Willman et al. 2012).

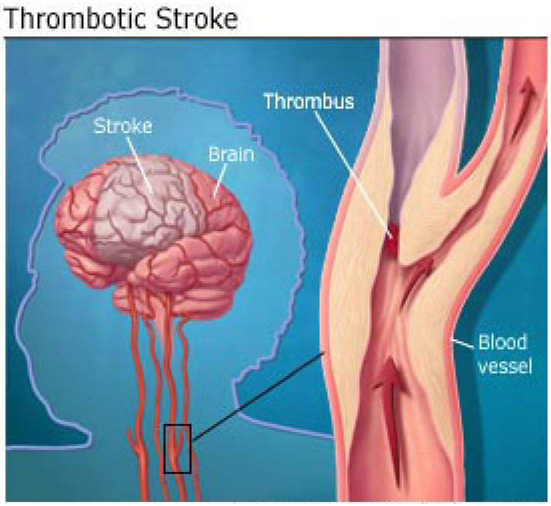

Figure 2.1 Illustration showing the etiology of thrombotic stroke in humans

Image adapted from (http://www.strokecarenow.com/stroke-information/)

Reperfusion of the ischemic brain area is an important goal in stroke treatments, either by intravenous medical treatments or endovascular procedures. Tissue plasminogen activator (tPA) has become the standard treatment for thrombolysis since its approval by FDA in 1996 (Zivin 2009). tPA is also known as IV-rtPA because it's usually administered through an IV in the arm. Although studies have shown that tPA administered within 4.5 hours of onset may improve the outcome of stroke patients (Davis and Donnan 2009), the relative short therapeutic window of tPA efficacy, dissolving blood clots in large vessels and the potential risk of intracranial hemorrhage has led to studies on improving the current treatment protocol. Researchers have been developing new thrombolytic agents or are combining tPA with a variety of anti-platelet agents in preventing re-occlusion of blood vessels. Aspirin, a commonly used antiplatelet agent, was combined with IV-rtPA in after onset of stroke, but the combined therapy showed no improved outcomes a higher risk of symptomatic intracranial hemorrhages (Zinkstok, Roos et al. 2012).

Cathepsin G (CatG) is a neutral proteinase with gene expression restricted to cells of the myeloid lineage (Burster, Macmillan et al. 2010), including neutrophils, monocytes, macrophages and microglia. The major source of CatG in circulating blood is neutrophils. Its association with excessive inflammatory reactions links CatG to a possible target for tackling ischemic brain injury. Previous studies have shown that CatG plays a role in both hemostasis(Sambrano, Huang et al. 2000, Shao, Wahrenbrock et al. 2011) and immune-related events (Pham 2006, Burster, Macmillan et al. 2010). CatG has been reported to cleave protease activated receptor-4 that is highly expressed in platelets (Sambrano, Huang et al. 2000). CatG has also been shown to be a potential strong platelet activator in vitro (Selak, Chignard et al. 1988). Recently, it was reported that ‘neutrophils modulate platelet activation and thrombus formation in vivo in a CatG-dependent manner’ (Faraday, Schunke et al. 2013).

Here, we propose a new mechanism for ischemic brain injury in which cathepsin G fosters cerebral thrombus formation by interacting with blood platelets. We designed two experiments to study the role of CatG in a novel atherothrombotic stroke model. In this model, the stroke is induced by a series of collagen injections through the carotid artery. First, we hypothesized that the deficiency of CatG would reduce intravascular thrombus formation during the injections of collagen, leading to a decreased magnitude of brain injury during the onset stroke period (**Experiment 1**). We also hypothesized that the combined treatment of tPA and a pharmacologic inhibitor of CatG would improve the outcome after stroke, promoting recovery of cerebral blood flow and reducing anatomic and behavioral brain injury (**Experiment 2**).

2.2 Materials and methods

2.2.1 Experiment design

A novel murine model that has similar pathophysiology to atherothrombotic stroke in humans was used in this study. Detailed characterizations of this model can be found in a previous publication (Schunke, Toung et al. 2015). Briefly, the new atherothrombotic stroke model was compared with the standard middle cerebral artery occlusion (MCAO) model, in which the MCA was occluded mechanically by a filament. The new model produced brain injuries similar in magnitude and variability with the conventional MCAO model. However, several mechanisms were included in the new method, such as intravascular platelet activation, cerebrovascular thrombus formation in situ, and persistent plaque instability, which better mimics the etiology of clinical ischemic stroke than the MCAO model.

2.2.1.1 Function of cathepsin G in thrombus formation

To test the function of CatG in thrombus formation, two groups of mice were used in this study: Group 1, Male C57BL/6 mice (n=2) as the wild type (WT); Group 2, Cathepsin G deficient (CatG-/-) mice (n=2) that were backcrossed for 10 generations on a C57BL/6 background.

2.2.1.2 Inhibition of cathepsin G with tPA in recanalization

Four experimental groups were designed to characterize the treatment effects of CatG inhibitor (CatGI) and/or tPA in this stroke model: 1) vehicle-control, 2) CatGI, 3) tPA, 4) combined CatGI + tPA. Twenty-four male C57BL/6 mice were randomly divided into the four groups. Each group was treated with the group-specific drugs (e.g. saline and DMSO for vehicle-control) through the internal carotid artery (ICA) 60 minutes after the first injection of collagen. Animals were sacrificed three hours post-collagen injection for histological validation.

2.2.2 Mouse model of atherothrombotic stroke

All experiments in this study were approved by the Johns Hopkins University Animal Care and Use Committee. Male C57B1/6 mice (25-30g; 3-4 months) were selected for this experiment. First, a thinned-skull window preparation was performed to allow optical access to the cortical vessels. The animal was anesthetized with an intraperitoneal injection of ketamine (100mg/kg) and xylaxine (10mg/kg). Ocular lubrication ointment was applied to the eyes to prevent corneal drying due to anesthetics. No surgical procedure was started until the pinch response disappeared, which indicated an adequate degree of anesthesia. The fur above the scalp was removed by gently scrubbing a cotton applicator with sensitive hair removal cream (Veet, Reckitt Benckiser, Parsippany, NJ, USA). The exposed scalp was first sterilized with ethanol and betadine, and then an incision was made to expose the skull of the right hemisphere between bregma and lamda. The connective tissue attached to the skull was removed by scraping the skull with a blunt surgical blade. After this, a high-speed dental drill with 1.4

mm diameter drill bur was used to thin the skull. The thinning was performed mainly on middle cerebral artery (MCA) and anterior cerebral artery (ACA) regions. Saline was perfused regularly between drilling to avoid heating. Drilling was stopped when cortical vessels could be visualized under a surgical microscope. After thinning the skull, the animal was fixed to a home-built stereotaxic frame for baseline imaging.

Then the animal was transferred to the surgical bench for preparations of collagen injection. The method in (Schunke, Toung et al. 2015) was modified by reducing the total injections of collagen from six to four and adding two infusion periods of CatGI and tPA as the treatment period. The animal was anesthetized using 1-2% isoflurane/30% O_2 with a body temperature maintained at 37.0 ± 0.5°C. The right neck and carotid bifurcation were dissected. The external carotid artery and right carotid artery were ligated, and the external carotid artery was used as a stump for passage of a PE8 catheter (SAI Infusion Technologies, Lake Villa, IL). The PE8 catheter was advanced into the internal carotid artery (ICA) approximately 5 mm past its bifurcation with the external carotid. A 10-µl Hamilton syringe was used to inject 1 µg of collagen (1 µg/µl, Chrono-Log Corp., Havertown, PA, USA) through the catheter four times at 5-min intervals. After 60 min of the first injection of collagen, the previous syringe was replaced with a 100-µl Hamilton syringe attached to the same catheter. Cathepsin G inhibitor (CatGI; dissolved in total volume of 10 µl saline and DMSO for a final concentration of 500nM in the mouse) or vehicle (5 µl saline and 5 µl DMSO) was infused through the ICA for 5 min. Right after the first infusion, tissue plasminogen activator (tPA, 10 mg/kg; Activase; Genentech, San Francisco, CA, USA) or vehicle control (11mg L-arginine, 3.14 mg phosphoric acid, 0.04 mg Polysorbate 80 dissolved in 100 µl distilled water) was infused through the ICA for 30 min. The carotid artery was reperfused immediately after the second infusion, by withdrawing the catheter and releasing the temporary carotid ligature. After the neck was sutured, animal was monitored for an additional 150 min using LSCI and fluorescence imaging.

For the experiment to determine the role of CatG in thrombus formation (**Experiment 1**), CatG deficient mice were used instead of male C57B1/6 for group 1 and compared with wild type animals. Also, no infusion was performed in experiment 1, the reperfusion was initiated right after the post-injection monitoring. The timeline for the *in vivo* imaging experiment is illustrated in **Table 2.1**, the flow chart is not scaled with respect to the actual experiment time.

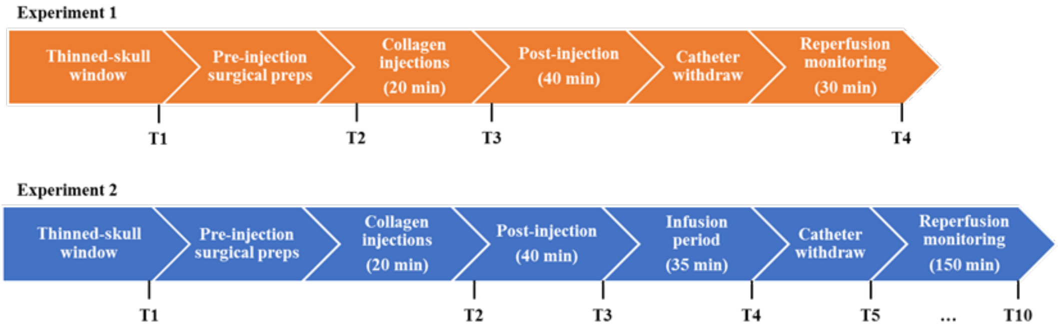

Table 2.1 Timeline for *in vivo* stroke imaging experiments

The blocks do not represent the actual time in each experiment step. T stands for time point. A number of time points were selected for further analysis of CBF changes and thrombi quantification.

2.2.3 Real-time fluorescence imaging of thrombus formation

Platelets were labeled *in vivo* before the surgical preparations for collagen injection. A fluorescently labeled IgG derivative X488 against the GPIbβ subunit of the murine platelet-specific GPIb-V-IX complex (0.4 μg/g, Emfret Analytics, Eibelstadt, Germany) was used via retro-orbital injection. This antibody is non-cytotoxic, does not alter platelet adhesion or aggregation *in vivo*. The labeled platelets would not exhibit fluorescence signal in its native state. X488 has been used in intravital analysis of platelet-involved pathological processes, such as thrombosis (Falati, Gross et al. 2002). A standard FITC-fluorescence filter set can then be used to visualize the aggregated platelets during thrombus formation.

2.2.4 Multi-modality imaging system for real-time monitoring of CBF changes during thrombus formation

A schematic of the imaging system used for this study is shown in the **Fig 2.2.** A red He-Ne laser beam (λ =632nm, Thorlabs, Newton, New Jersey, USA) was first expanded and then used for illumination during LSCI. A blue laser (λ =473nm, Cobolt, Solna, Sweden) was used to excite the FITC-labeled fluorescent antibody. The two light sources were turned on sequentially during each imaging session. A macro lens (Nikon, Melville, New York, USA) included with this system had a focal length of 60 mm and a maximum *f-number* of 2.8. This system has a magnification of 1.4. A long-pass filter (cutoff wavelength=496nm, Semrock, Rochester, New York, USA) was also incorporated into this system to prevent the blue excitation light from entering the camera while simultaneously allowing green fluorescence light and red light for LSCI to pass. Images for both

LSCI and fluorescence imaging were acquired using the same 16-bit CCD camera (Infinity 3-1, Lumenera, Canada) with a 1024 × 1396 pixel sensor and a maximum frame rate of 12.5 fps. Image acquisition was performed by a custom-designed software in MATLAB.

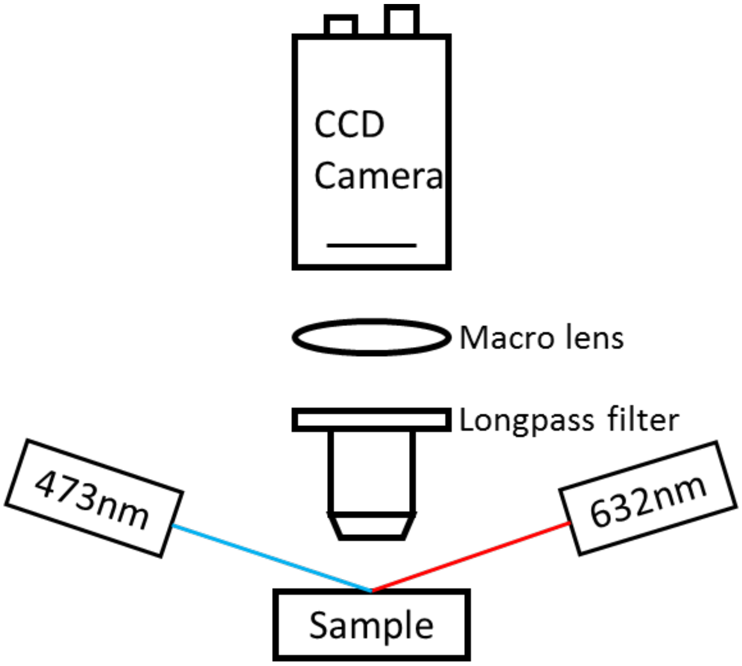

Figure 2.2 Schematic of the multi-modal optical imaging system.

The mouse was anesthetized with isoflurane and head-fixed to a stereotaxic frame. Two laser light sources were turned on sequentially to acquire laser speckle and wide-field fluorescence images.

2.2.5 Image acquisition and analysis

2.2.5.1 Image acquisition

Raw laser speckle images were acquired using the Lumenera CCD camera at 5 ms exposure time and at frame rate of 12.5 fps. 80 raw images were used to construct one LSCI image by the temporal processing scheme (Cheng and Duong 2007). Relative flow maps ($1/\tau_c$ maps) were calculated using the $1/K^2$

approximation as described in Chapter 1. Fluorescence images were acquired using the same camera at 200 ms exposure time.

2.2.5.2 Image registration

Since the right hemisphere of mouse's brain underwent a large stroke due to the injections of collagen and the mouse had to be removed from the imaging bench several times for surgical preparations, the intensity profile of LSCI images changed drastically across different time points. These signal intensity changes occurred both within the region of interest (from the stroke) and the background region (due to motion). These concurrent signal changes make it challenging for conventional automated image registration tools to successfully register the images in each experimental time course. Therefore, images across different time points were manually registered using a rigid body transformation based on the landmarks placed on common vessels. The result of manual image registration is illustrated in **Fig 2.3**. An enlarged view of a selected vascular region is marked by the red box and the difference image (Fig 2.3(a) minus Fig 2.3(b)) of that ROI is shown in **Fig 2.3(c)**. As clearly pointed by the color arrows in the difference image, two identical vasculature patterns are shown in the difference image, which indicates that the two LSCI images are misaligned due to motion. The difference image after registration is shown in **Fig 2.3(f)**, the two images are well-aligned and only one vasculature pattern is shown. The white appearance of the vessels in **Fig 2.3(f)** comes from the flow difference between the two experimental time points.

However, for registering the images within the reperfusion period, there were situations that neither huge vasculature changes nor motion artifacts occurred. In those cases, an automatic intensity-based registration was performed also using a rigid body transformation (Thevenaz, Ruttimann et al. 1998).

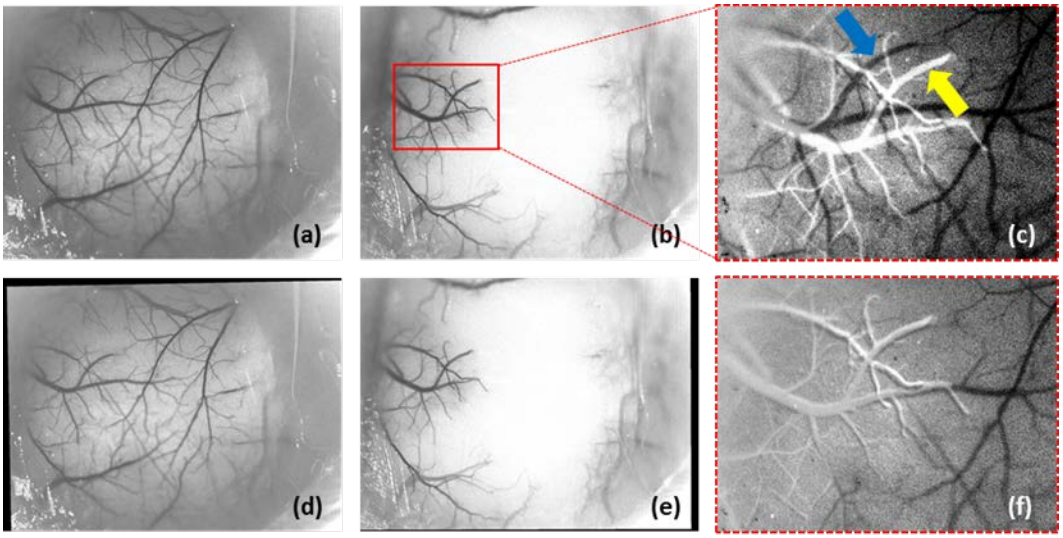

Figure 2.3 Manual registration of LSCI images across different time points.

(a) Un-registered LSCI image of T1 (baseline). (b) Un-registered LSCI image of T6 (30 minutes after reperfusion). (c) An enlarged view of the difference image (between a & b), the colored arrows illustrate the displacement between two experimental time points. (d) Co-registered LSCI image of (a). (e) Co-registered LSCI image of (b). (f) The same difference image after registration. All images except the difference images (c & f) are shown by the scale of 0 to 0.3.

2.2.5.3 Vessel segmentation

The image processing steps that constitute the blood vessel segmentation pipeline are summarized in the flowchart below (**Fig 2.4**). Briefly, a tubeness filter was employed to enhance the curvilinear structures (e.g. vessels) in the LSCI images (Sato, Nakajima et al. 1998). This filter calculates how 'tube-like' each pixel in the image is, which uses the eigenvalues of Hessian matrix to measure ‘tubeness’. It first convolves the image with a spherical Gaussian kernel with standard deviation of σ. The filter responses can be tuned to vessels of different diameters by adjusting the value of σ. To obtain a multi-scale image which accommodates both macro- and micro-vessels, results of using different tubeness filters were combined using a pixel-wise ‘maximum’ operation in ImageJ (Schneider, Rasband et al. 2012).

Since blood vessels appear dark on LSCI images, and the tubeness filter in ImageJ requires bright vessel structures, the LSCI image was first inverted before further processing. When using a small σ value, blood vessels are more easily connected with background noise, which introduces unwanted artifacts in the following threshold step. On the other hand, a large σ value results in unwanted dilation of small vessels. Therefore, we optimized the tubeness filter set to $\sigma = 2$, 3, 4 in this processing scheme by visual inspection. The outputs of three filters were combined by choosing the max intensity among the three (max intensity command under Z project in ImageJ). Manual intensity threshold (IJ_IsoData) was applied to the ‘max’ result, and resulted in an initial binary vascular structure map. Extensive care was taken to ensure that the manual thresholding was the best representation of the LSCI image. A region removal filter was applied to eliminate small, disconnected objects in the binary vascular map. Furthermore, the binary vascular map was compared with the LSCI image, and any ‘non-vascular’ structure and image artifact was removed by manual masking. These image processing steps are illustrated in **Fig 2.5**.

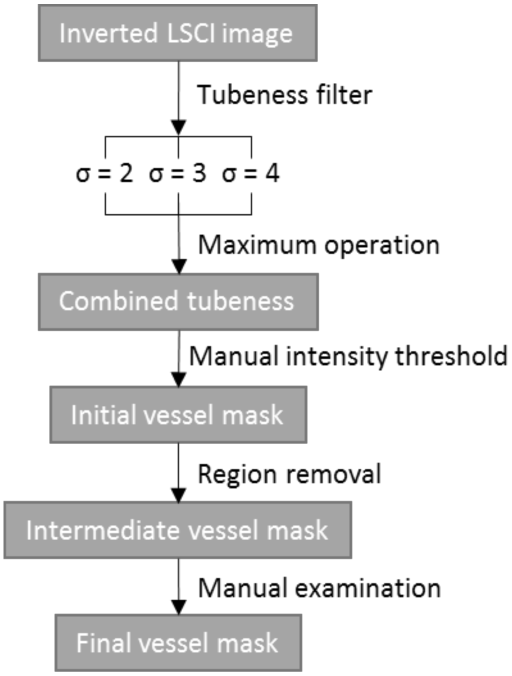

Figure 2.4 Flow chart of blood vessel segmentation procedures.

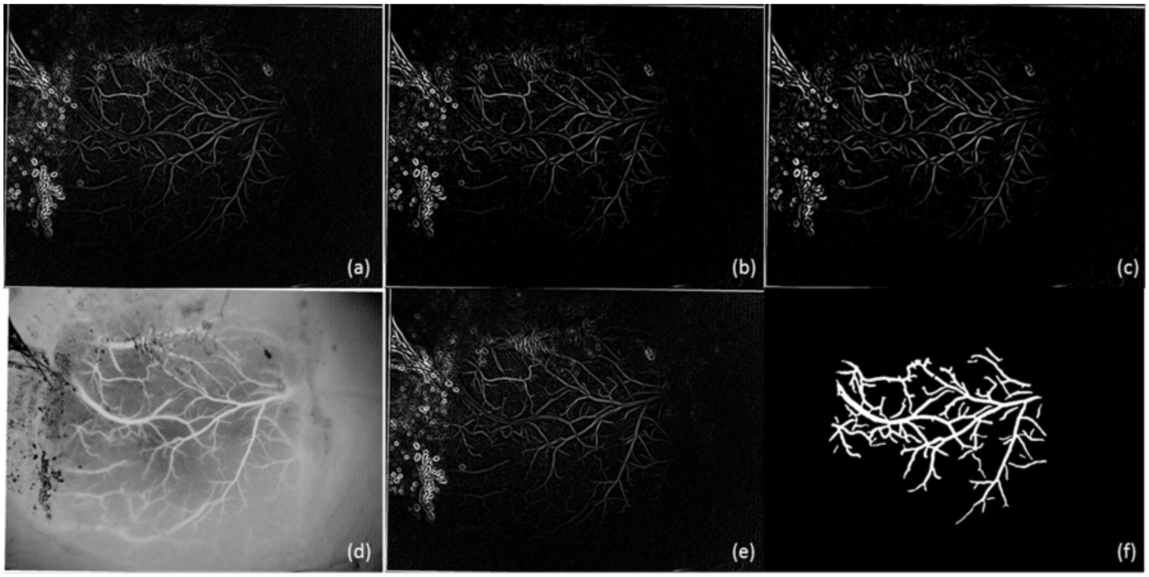

Figure 2.5 Representative images of vessel segmentation procedures

(a-c) Inverted LSCI image of (d) after tubeness filtering (σ = 2, 3, 4). (d) Inverted LSCI image, showing by a scale of 0.7 to 1. (e) Combined tubeness filtered image, after max operation of (a-c). (f) Final vessel segmentation mask from (e).

2.2.5.4 Cerebral blood flow calculation

Several methods of quantifying cerebral blood flow (CBF) from LSCI images can be found in (Hecht, He et al. 2012, Liu, Li et al. 2014). In (Hecht, He et al. 2012), the relative CBF was calculated by the summation of all the flow values within a rectangular region of interest (ROI). This method did not separate vessels from the background region, so day to day physical alterations of the skull from could introduce variability in CBF. In (Liu, Li et al. 2014), a photothrombotic stroke model was used, where only one major branch of MCA was occluded by green light illumination. Because of the localized stroke region, the change of CBF was quantified by small ROIs within the targeted vessel. Due to the difference in their stroke model and ours (injections of collagen induce a global stroke), the above-mentioned method for analyzing photothrombotic stroke could not be applied to our CBF calculation.

Also, to eliminate the confounding effect of background changes, we propose a new CBF calculation method for the atherothrombotic stroke model. The vessel segmentation result was combined with the flow distribution map for CBF calculation. Only the areas categorized as vessels were taken in to account in the CBF calculation. Instead of analyzing the small ROIs in the photothrombotic stroke, the global CBF change could be analyzed by including all the visible vessels within the field of view (4 mm × 4 mm). One possible advantage of this method could be that more details of the CBF change could be analyzed. We divided the vessels into two regions, MCA territory and ACA territory (shown by the white dotted lines in **Fig 2.6**), which allowed us to separate the CBF responses from the two territories. Further processing of the vessel segmentation result could lead to vessel diameter calculations, from that, the characteristics of CBF changes among vessels of different diameters (e.g. macro-, intermediate and micro-vessels) could then be studied separately.

2.2.5.5 Thrombus quantification

A fine grid was applied to the fluorescence image. The thrombus was quantified by the total number of overlaps between the grid and fluorescence thrombi.

2.2.6 Statistical analysis

Data are expressed as mean ± s.e.m (standard error of mean) and were analyzed by ANOVA. All testing was two-tailed, and results were considered significant at $P < 0.05$.

2.3 Results of testing the role of CatG in thrombus formation (Experiment 1)

2.3.1 CBF changes between WT and CatG−/− mice

The relative CBF distribution maps were generated from LSCI images using the $1/K^2$ approximation. Since speckle contrast originates from moving red blood cells inside cortical vessels, occluded vessels from stroke will not show up in the CBF distribution maps. Four experimental time points were selected for further CBF analysis: (T1) baseline; (T2) 5 min after 1st injection of collagen; (T3) 5 min after 4th injection of collagen; and (T4) 30 min after reperfusion. These time points are annotated in the time line (**Table 2.1**). CBF flow distributions between the two groups are shown in **Fig 2.6**. The CBF trend in **Fig 2.7** was calculated as a percentage of baseline CBF values. More clearly shown in the CBF distribution maps, the wild type mouse experienced a larger decrease in CBF than CatG deficient mouse after collagen injections. When comparing the flow after 4th injection (T3) between WT and CatG -/-, we can clearly see that some flowing blood vessels could still be visualized in the CatG deficient group, where no flow could be seen in the wild type group. Same conclusion can be made for the flow distributions at 30 min after reperfusion (T4).

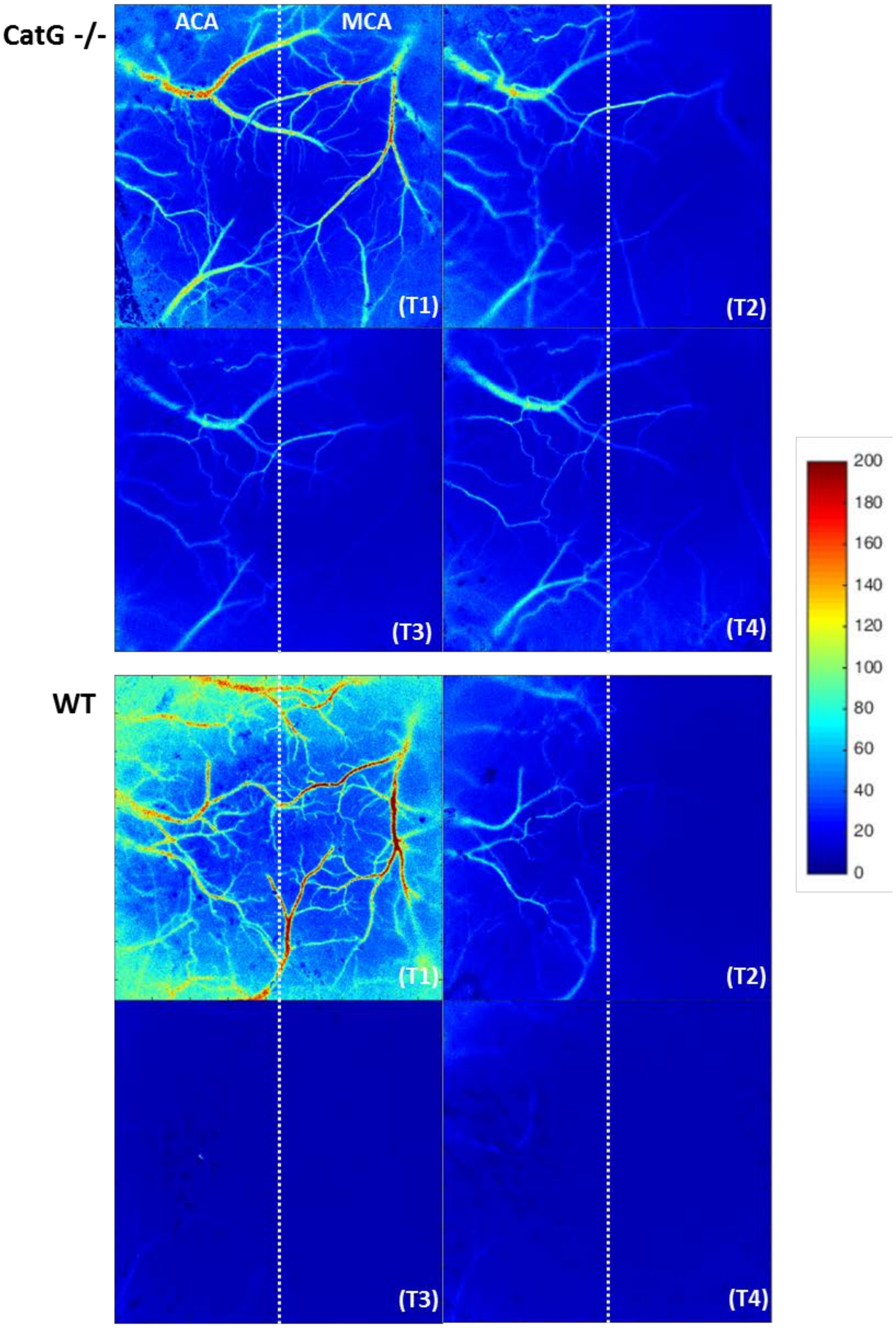

Figure 2.6 CBF distribution maps between CatG deficient and wild type mouse by LSCI

Four time points are shown in this figure for CBF analysis: (T1) Baseline image. (T2) 5 min after 1st collagen injection. (T3) 5 min after 4th collagen injection. (T4) 30 min after reperfusion. The color bar is showing the relative CBF values, a higher value (approaching red colors) indicates a higher blood low.

We also grossly separated the flow maps into ACA and MCA territories by drawing a center-line through the flow distribution maps (**Fig 2.6(a)**). Different characteristics of CBF changes could be seen between ACA and MCA territories by **Fig 2.7(b-c)**. MCA territory experienced a larger decrease in CBF, which agrees with the stroke model wherein collagens were injected proximally to the opening of MCA and thus, MCA branches were more likely to be affected by the thrombi than ACA branches.

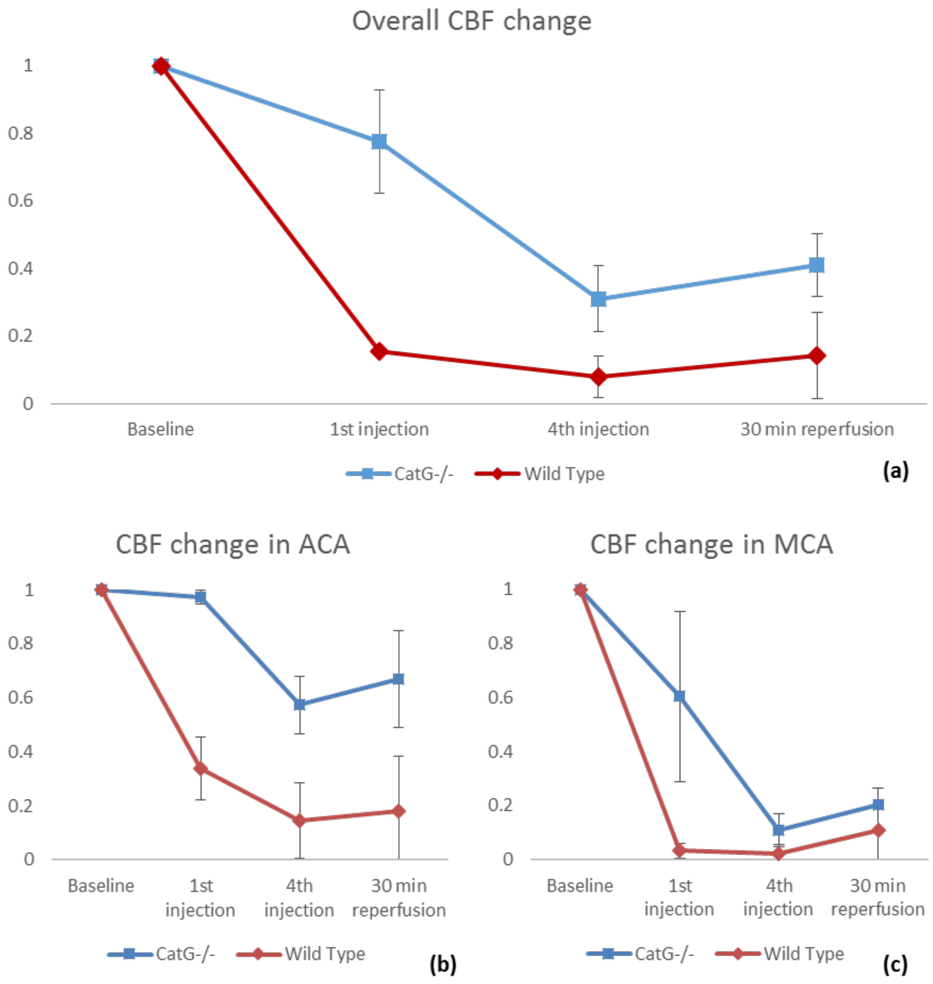

Figure 2.7 CBF changes between wild type and CatG deficient mice (as percentage of baseline)

(a) Overall CBF comparison. (b) CBF comparison in ACA. (c) CBF comparison in MCA.

2.3.2 Thrombus formation between WT and CatG−/− mice

Fig 2.8 shows the fluorescence images of aggregated platelets at 5 min after 4th collagen injection. In these fluorescence images, thrombi were labeled by the X488 antibody and appear bright in the gray-scale images (highlighted by the red arrows). Vessels that do not have thrombi appear dark in these images. When comparing the two genotypes (wild type and CatG -/-) , a much larger portion of cortical vessels in the MCA branch were seen to be clotted in the wild type mouse than the CatG deficient mouse (**Fig 2.8**).

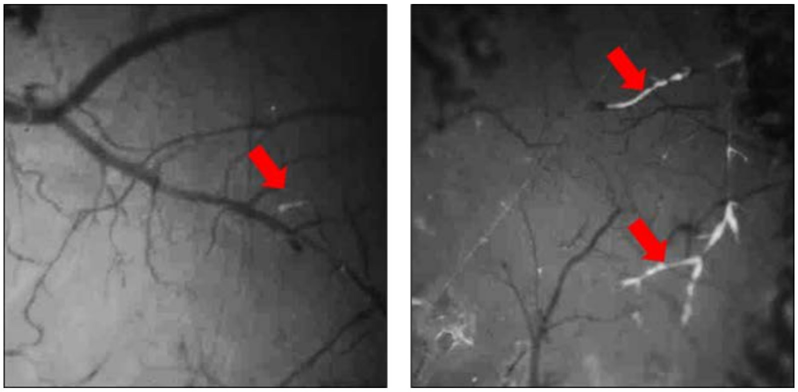

Figure 2.8 Representative FITC-fluorescence images of thrombi from *in vivo* platelets labeling

(Left) Fluorescence image from a CatG -/- mouse. (Right) Fluorescence image from a wild type mouse. The red arrows indicate thrombi locations.

2.4 Results for the effects of CatGI and/or tPA treatment (Experiment 2)

2.4.1 CBF changes following CatGI and/or tPA therapy

To quantify the efficacy of CatGI and/or tPA therapy in the recanalization after the stroke, a total of ten time points were used for further CBF analysis: (T1) baseline; (T2) 30 min after 1st collagen injection; (T3) 60 min after 1st collagen injection; (T4) the end of 2nd infusion (either vehicle or tPA), (T5) immediate after reperfusion; (T6) 30 min after reperfusion; (T7) 60 min after reperfusion; (T8) 90 min after reperfusion; (T9) 120 min after reperfusion; and (T10) 150 min after reperfusion. These time points are annotated in the time line of experiment 2 in **Table 2.1**.

Representative CBF distribution maps of the four experimental groups are shown in **Fig 2.9** for selected time points (T1, T3, T4, T6, T9 and T10). The CBF in vehicle-control group stayed constant throughout the experiment period, with CBF values of 23.16% ± 1.24% (mean ± standard deviation) of baseline during the reperfusion period (between T4 to T10). In the three treatment groups, different magnitudes of CBF recovery could be seen during the reperfusion period. Some blood clots were resolved by the infusion treatment, with signs of flow resumption/increase in some blood vessels (highlighted by the white boxes in CatGI group images), and/or reconnection of different blood vessel branches (highlighted by the white boxes in combined group images). Especially in the combined CatGI + tPA therapy group, a 27.38% increase in CBF was seen when comparing time point 4 with 10 (150 min reperfusion).

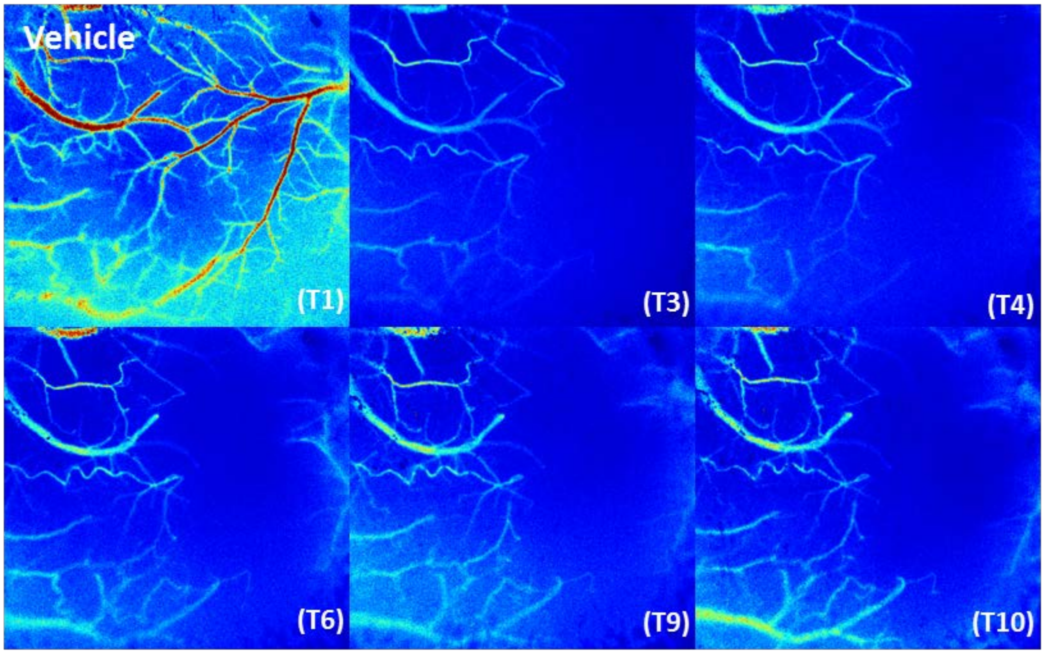
Vehicle
(T1)
(T3)
(T4)
(T6)
(T9)
(T10)

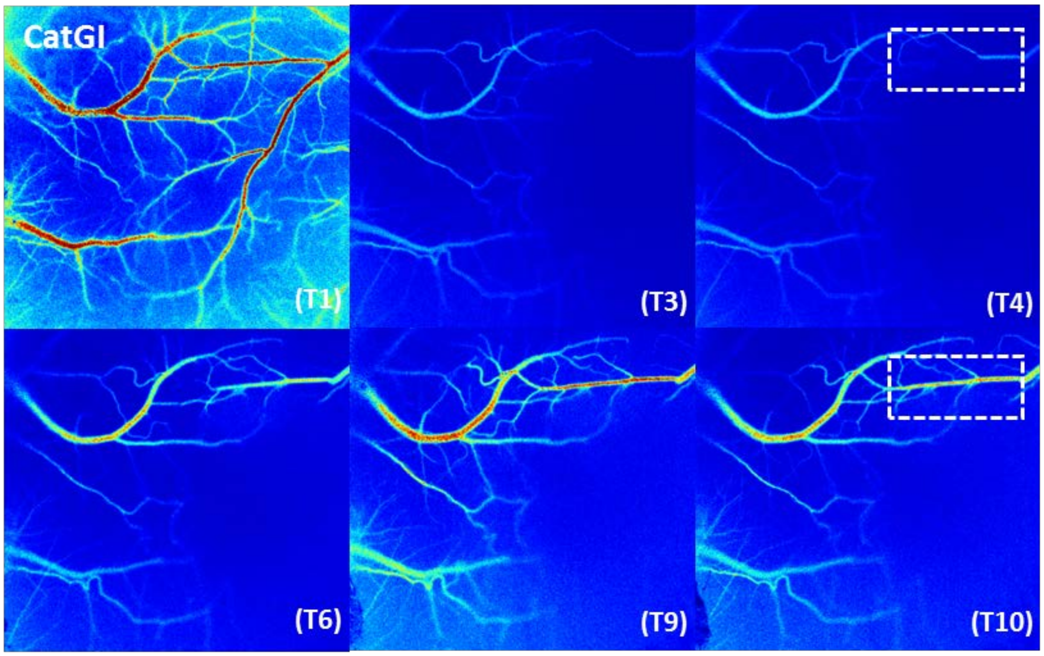
CatGI
(T1)
(T3)
(T4)
(T6)
(T9)
(T10)

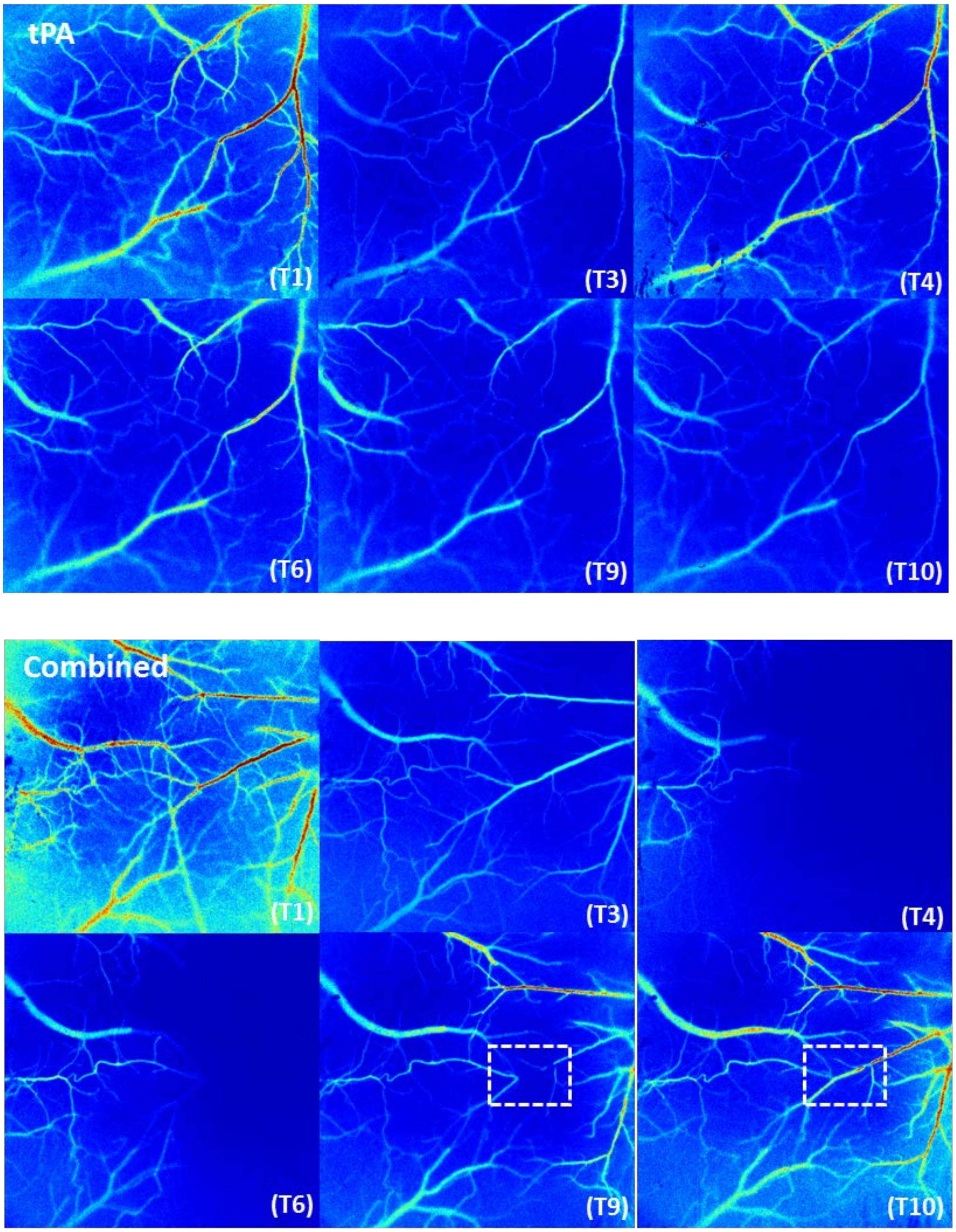

Figure 2.9 Representative CBF distribution maps of the four experiment groups

Six time points are selected to illustrate the CBF changes from collagen injections and treatment during reperfusion: (T1) Baseline. (T3) 60 min after 1st injection. (T4) After 2nd infusion. (T6) 30 min after reperfusion. (T9) 120 min after reperfusion and (T10) 150 min after reperfusion.

The relative CBF change (as a percentage of baseline) among the four experiment groups is shown in **Fig 2.10**. At time point 10, the mean CBF of combined treatment group was significantly higher than the vehicle control group.

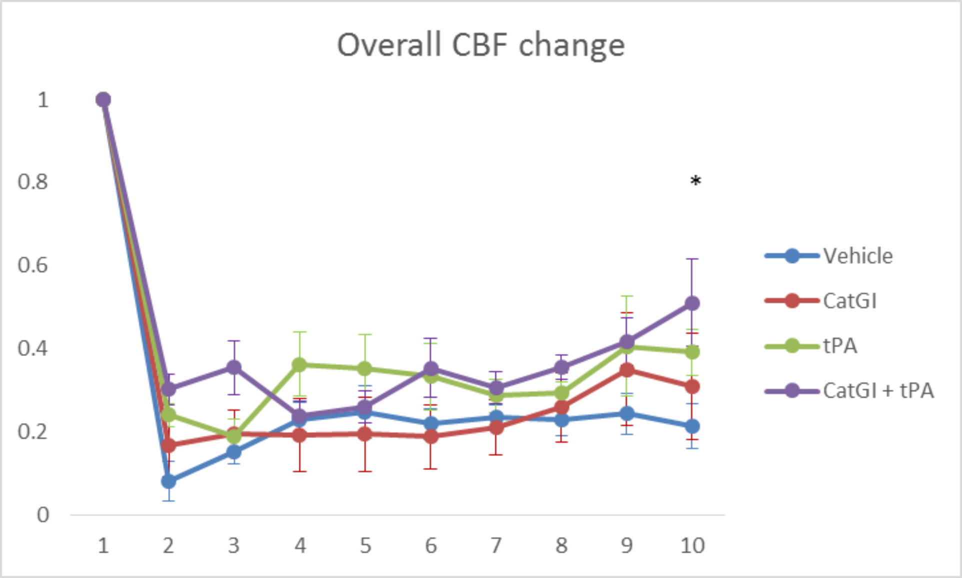

Figure 2.10 CBF changes of the experiment groups in selected time points

(T1) baseline; (T2) 30 min after 1st collagen injection; (T3) 60 min after 1st collagen injection; (T4) the end of 2nd infusion (either vehicle or tPA), (T5) immediate after reperfusion; (T6) 30 min after reperfusion; (T7) 60 min after reperfusion; (T8) 90 min after reperfusion; (T9) 120 min after reperfusion; and (T10) 150 min after reperfusion.

2.4.2 Perfused area change in CatGI and/or tPA therapy

We further separated the changes in CBF using results from the vessel segmentation to compute the total 'perfused' area. Perfused area indicates the area that was perfused by blood vessels, and may also be an *in vivo* marker of quantifying core/penumbra of the stroke. The perfused area was calculated by counting the number of pixels classified as vessels in the vessel segmentation results. As shown in **Fig 2.11**, the combined treatment of tPA + CatG significantly improved the perfused area at 150 min after the start of reperfusion (T10).

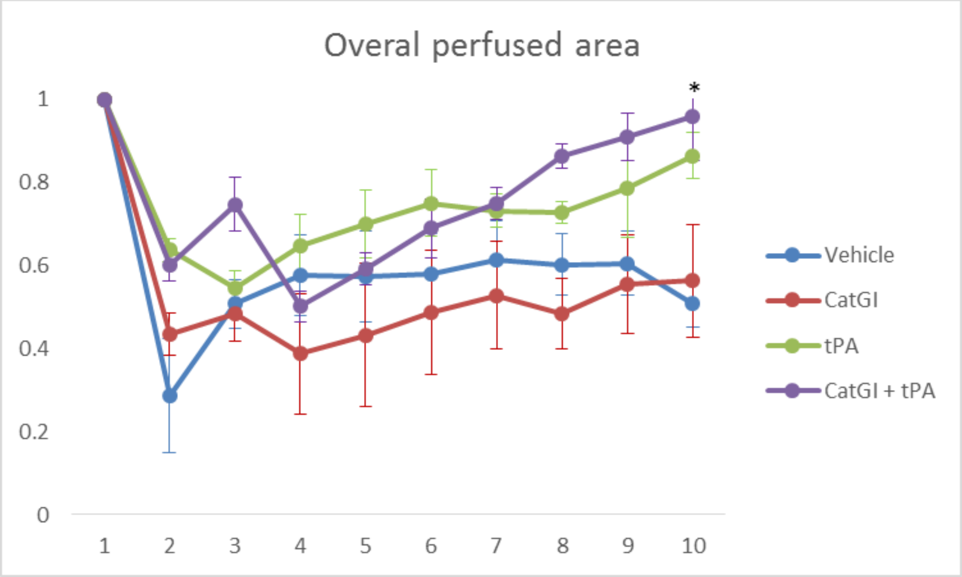

Figure 2.11 Overall flow area changes of the experiment groups in selected time points

2.5 Discussions

Improved CBF and perfused area in the combined treatment group suggest that the combined tPA+CatGI treatment might improve the reperfusion and neurological outcome of this stroke model.

We also performed histology, immunohistochemistry and immunofluorescence analysis to quantify the penumbra area, thrombi and infract volume, respectively. An example of infarct volume comparison between vehicle and CatGI treatment is shown by **Fig 2.12**. However, due to the time restraint, we are not able to present the results before the submission of this thesis. Future work of this project will be comparing the results from histology analysis with the CBF/flow area from LSCI, and determine the sensitivity/accuracy of *in vivo* LSCI imaging in predicting histology analysis.

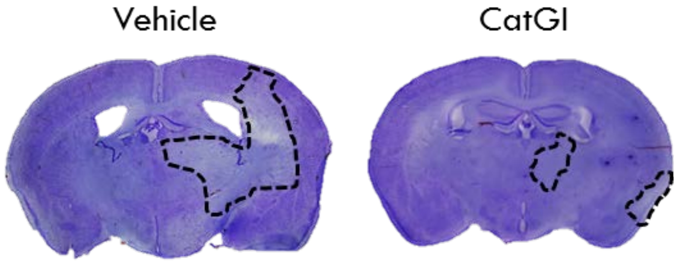

Figure 2.12 Cresyl Violet staining for infarct volume calculation between vehicle and CatGI. The dotted black lines indicate the infarct areas.

CHAPTER 3 EFFECTS OF CRANIAL WINDOW TYPES ON MONITORING NEUROVASCULATURE USING LASER SPECKLE CONTRAST IMAGING

3.1 Introduction

Optical imaging tools (e.g. two-photon microscopy, optical coherence tomography, laser speckle contrast imaging) provides much higher temporal and spatial resolution than MRI and PET, which allows researchers to capture rapid biological changes at a much finer scale. When it comes to neuroimaging, details of the brain physiological parameters, such as cerebral blood flow from individual vessels, Calcium activities from individual neurons can be obtained by optical imaging tools. However, the imaging depth and spatial resolution of optical neuroimaging tools are limited by the large light scattering from the scalp and cranium. In preclinical models, optical cranial window is usually performed to address this issue.

Two types of cranial windows are commonly employed for rodent neurophysiological studies: (i) thinned-skull and (ii) open-skull (or craniotomy) preparations. In the thinned-skull preparation (Yang, Pan et al. 2010), skull section above the region of interest (ROI) is thinned down to a thickness of ~ 15 to 20 μm. In contrast, in an open-skull preparation, that area of the skull would be completely removed and replaced with a glass coverslip (Holtmaat, Bonhoeffer et al. 2009). Depending on the purpose of study and complexity of the surgery, investigators may prefer one window preparation to the other. Cranial windows have been used in a variety of chronic in vivo studies of synaptic plasticity (Trachtenberg, Chen et al. 2002) vascular progression after ischemic stroke (Schrandt, Kazmi et al. 2015), etc. The animals implanted with cranial window were allowed to recover for a certain time period before imaging. However, in most of the acute studies, the animal were immediately transferred to experiments after window implantation (Masino, Kwon et al. 1993). Issues such as the potential inflammatory response/cerebral blood flow changes from cranial window preparation cannot be opted out from the experiment results. Hence, there is a strong need to investigate the effects of cranial windows on imaging outcomes. While an evaluation of the effect of cranial window type for two-photon laser scanning microscopy (2PLSM) has been reported (Isshiki and Okabe 2014), this study only revealed the effects on the optical resolution of 2PLSM, which does not apply to wide-field imaging techniques like LSCI. Also, the comparison between the two window types was performed in an acute experimental setting (Isshiki and Okabe 2014), which did not provide an assessment of the stability of the cranial window preparations for chronic imaging applications.

To the best of our knowledge the effect of cranial window type on image outcomes using LSCI has not been reported. Therefore, in this study, we investigated the effects of cranial window types on the ability of LSCI to characterize neurovascular structure and function. To do this we conducted longitudinal (i.e. chronic) in vivo imaging of mouse brain using the two window types continuously for fourteen days. The effect of window type on imaging outcomes was systematically assessed using parameters such as CNR (Contrast-to-noise Ratio) and MVD (Microvessel Density). Finally, we also quantified how window quality changed on a daily basis over two weeks.

3.2 Materials and Methods

3.2.1 Cranial Window Preparations

All in vivo experimental protocols used in this study were approved by the Johns Hopkins University Animal Care and Use Committee. Female athymic nude mice (6–8 weeks old) were divided into two groups: a thinned-skull window group (n = 5) and an open-skull window group (n = 5). Before creating the cranial window, mice were anesthetized with a mixture of ketamine (100 mg/kg) and xylazine (10 mg/kg). In order to reduce inflammation at the site of the cranial window, an intramuscular injection of dexamethasone (0.02 ml, 3 mg/ml) was administered before surgery (Holtmaat, Bonhoeffer et al. 2009). Also, a subcutaneous injection of carprofen (0.3 ml, 0.5 mg/ml) was administered after the surgery and after each imaging session.

A midline incision was made in the scalp to expose the skull between bregma and lamda fissures. For the thinned-skull preparation, a 3-4 mm diameter window was carefully thinned using a high-speed dental drill (AEU-10SS, Aseptico, Woodinville, WA, US). Sterile saline was perfused regularly during drilling to avoid heating the window site. Drilling was stopped when cortical vessels could be visualized under a surgical microscope. The scalp was then closed with wound clips (BD, Franklin Lakes, NJ, US). For the open-skull window preparation, a circular groove was drilled around the ROI. The circular skull fragment was then carefully removed using forceps. A 3 mm diameter round coverslip (Warner Instruments, Holliston, MA, US) was placed on the craniotomy area. Vetbond (3M, St. Paul, MN, US) was applied to the edge of coverslip to secure its position. The open scalp area was then covered with dental cement. All surgical procedures were performed using standard sterile precautions.

Finally, for the thinned-skull group, an open-skull window preparation was performed on the same ROI on day 14. This allowed the direct comparison between two window types for the same cortical region in each animal.

3.2.2 Image Acquisition

Animals were first anesthetized using a mixture of 3% isoflurane and room air, and then restrained in a home-built stereotaxic frame. Isoflurane was kept at 1–2% during the image acquisition. The imaging system for this study is shown in **Fig 2.2**, except that the blue laser for wide-field fluorescence imaging was not used in this study. A stack of 80 raw laser speckle images was acquired (5 ms exposure time) under 632.8 nm laser illumination (He-Ne laser, Thorlabs, Newton, NJ, US). LSCI images were generated using the temporal processing scheme (Cheng, Luo et al. 2003). The speckle contrast K for each pixel was calculated according to:

$$K = \frac{\sigma}{\mu}$$

Where σ and μ stand for the standard deviation and mean of the pixel values across the 80 images, respectively. Image acquisition was performed daily for 14 days on both groups.

3.2.3 Image Analysis

All the images in this study were analyzed using ImageJ (Schneider, Rasband et al. 2012) and MATLAB. Due to deterioration of the image contrast and disappearance of some blood vessels over time, it was challenging to employ an automated image registration algorithm. Therefore, LSCI images from each experimental time point were manually registered based on landmarks placed on common blood vessels. Manual vessel segmentation was performed for each LSCI image using a drawing pad. A representative of vessel mask (manual segmentation result) for day 2 of thinned-skull window image is shown in lower right panel of **Fig 4.3**. All the following image analysis was based on the co-registered LSCI images, ensuring that only the same vessel ROIs are taken into account. Unless otherwise noticed, all the data in this study are represented by mean ± s.e.m. Two paired t-test was used for all the statistical analysis, and $p < 0.05$ was considered as statistical significant.

3.2.3.1 Contrast-to-noise ratio

Contrast-to-noise ratio (CNR) is used as a metric to assess the ability to distinguish vessels from surrounding background regions. CNR is defined by

$$CNR = \frac{\mu_{background} - \mu_{vessel}}{\sigma_{background}}$$

Here, μ_{vessel} and $\mu_{background}$ are means of speckle contrast values in the blood vessel and background ROI, respectively. $\sigma_{background}$ is the standard deviation of the background ROI. For the CNR calculations, two different masks were generated to extract either the vessel or background ROI. The blood vessel mask was generated by manually segmenting the visible blood vessels using a drawing pad. Next, the LSCI image was logically multiplied with the blood vessel mask, and the result used as the vessel ROI. A morphological eroding of the vessel mask was performed to dilate the blood vessel mask and the difference between the eroded mask and the original vessel mask was used as the background mask. As a result, only the immediate background surrounding the blood vessels was used as the background ROI in all subsequent analysis.

3.2.3.2 Microvessel density and overall vessel length

Microvessel density (MVD) is an important metric employed in vasculature-related research, especially in studies on tumor angiogenesis (Hlatky, Hahnfeldt et al. 2002, Rege, V Thakor et al. 2012). Here we use MVD to assess the window quality. Traditionally, MVD was computed by counting individual microvessel segments in histology slides (Weidner, Semple et al. 1991). Due to the difference in image modalities, we modified the calculation of MVD by estimating the number of nodes within the segmented LSCI image (Rege, Seifert et al. 2012). A node was defined as either a junction of two vessel segments or the end point of a vessel segment within the field of view. All the MVD analysis was performed using the angiogenesis analyzer plugin for ImageJ (Carpentier, Martinelli et al. 2012). **Fig 3.1(a)** shows a representative manually segmented vessel ROI, and the corresponding MVD map from the angiogenesis analyzer plugin is illustrated in **Fig 3.1(b)**. **Fig 3.1(d)** shows a junction highlighted by a red arrow and an end point highlighted by a blue arrow in the zoomed out view of **Fig 3.1(b)**.

The total vessel length was another metric used to assess the window quality. The vessel maps were binarized and skeletonized. Next, the total blood vessel length within the ROI was calculated by adding together the total number of pixels categorized as blood vessels in the skeletonized map.

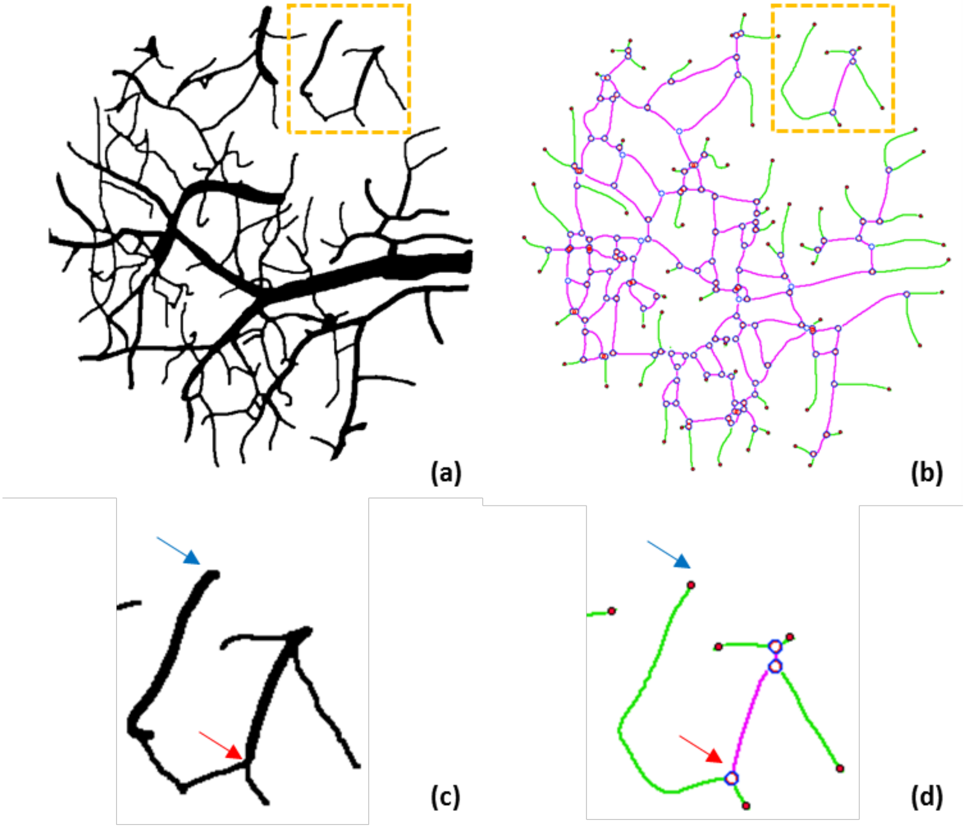

Figure 3.1 Vessel segmentation and corresponding microvessel density map computation

(a) Result of the semi-automated vessel segmentation from the LSCI image, the yellow box area is zoomed out in (c) to show the detailed vascular structure. (b) Microvessel density (MVD) map estimated from the image in (a). (c-d) are magnified views of the region within the yellow box in (a-b). End points are denoted by solid red circles and junctions are denoted by hollow blue circles in the MVD map. The green line represents a vessel segment delimited by an end point and a junction. The cyan line represents a vessel segment delimited by two junctions.

3.3 Results

3.3.1 Longitudinal LSCI images for open-skull and thin-skull window

The LSCI images from longitudinal monitoring of two window groups are shown in **Fig 3** and **Fig 4**. For the thinned-skull window group, open-skull preparation was performed on day 14 and the corresponding LSCI image with open-skull is shown in **day 14 image**. This allows a direct comparison between the two window types using the same ROI.

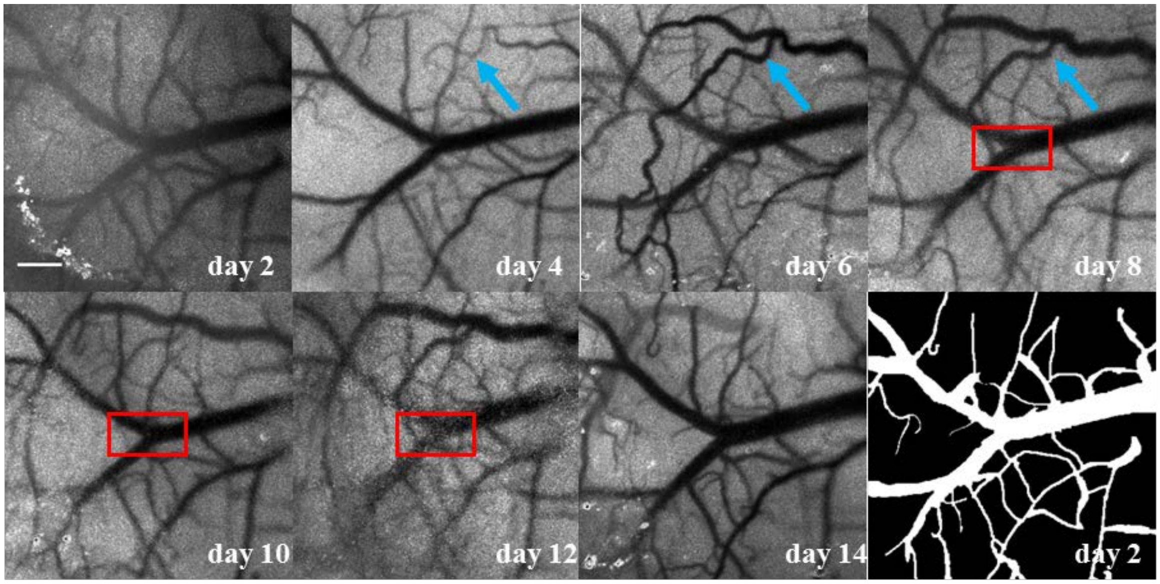

Figure 3.2 : Co-registered longitudinal in vivo LSCI images from a mouse bearing a thinned-skull window.

Images are shown from day 2 to day 14. On day 14, open skull preparation was performed over the same ROI. The binary image is the manual segmentation of day 2 LSCI image. The blue arrows illustrate the development of a new vessel. The red boxes show an example of skull regrowth acquired by LSCI images. Scale bar = 250 μm, and the scale applies to all the images in this figure.

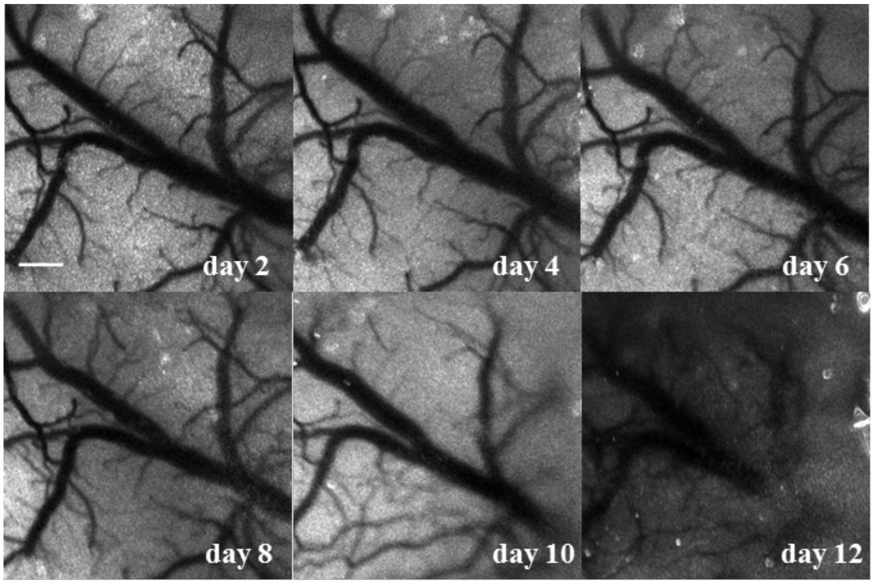

Figure 3.3 Co-registered longitudinal in vivo LSCI images from a mouse bearing an open-skull window

Images are shown from day 2 to day 12. Scale bar = 250 μm. The scale applies to all the images in this figure.

3.3.2 Contrast-to-noise ratio

To minimize the differences among individual subjects, the CNR of each mouse was normalized to its CNR value on day 2 for the open-skull group. To directly compare the CNR between thinned-skull and open-skull groups, the CNR of each mouse in thinned-skull group was normalized by its CNR value on day 14, when an open-skull window was created. As clearly shown by the CNR trend in **Fig 3.4**, the CNR in the thinned-skull group initially increased with time, after day 6, the CNR began to decrease over time. Contrary to that, a monotonic decrease in CNR was observed in the open-skull group.

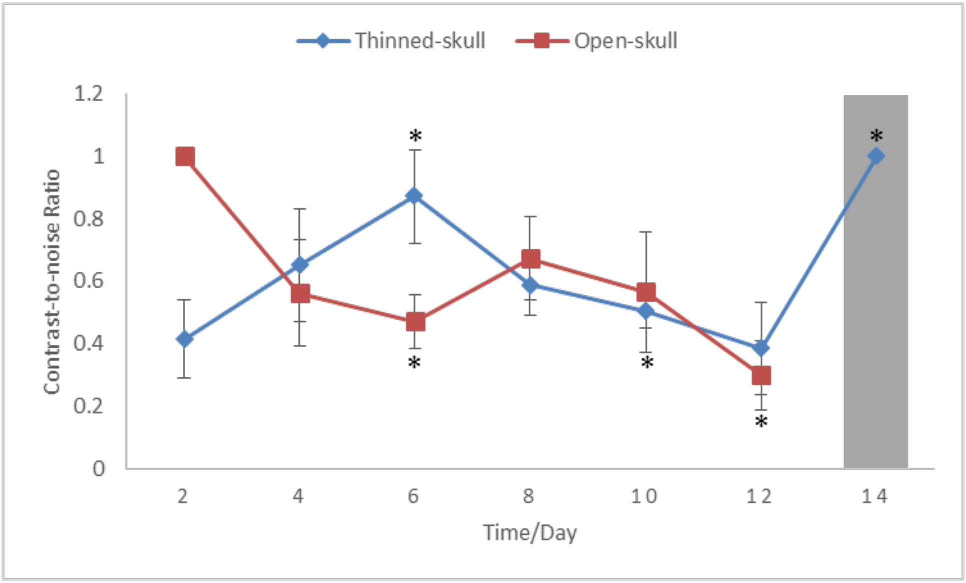

Figure 3.4 Normalized contrast-to-noise ratio between open-skull and thin skull windows

The colored area indicates that an open-skull preparation was performed on day 14.

3.3.3 Microvessel density

For the thinned-skull group, MVD initially increased. However, after day 6, the MVD began to decrease. For the open-skull group, a monotonic decrease in MVD was observed (**Fig 3.5(a)**). Total vessel length exhibited a pattern similar to MVD when comparing the two groups.

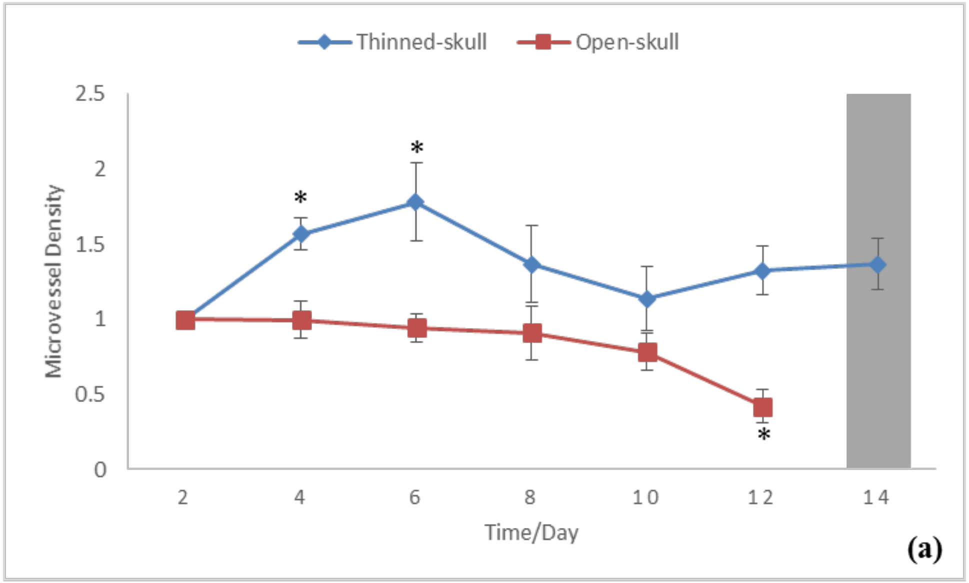

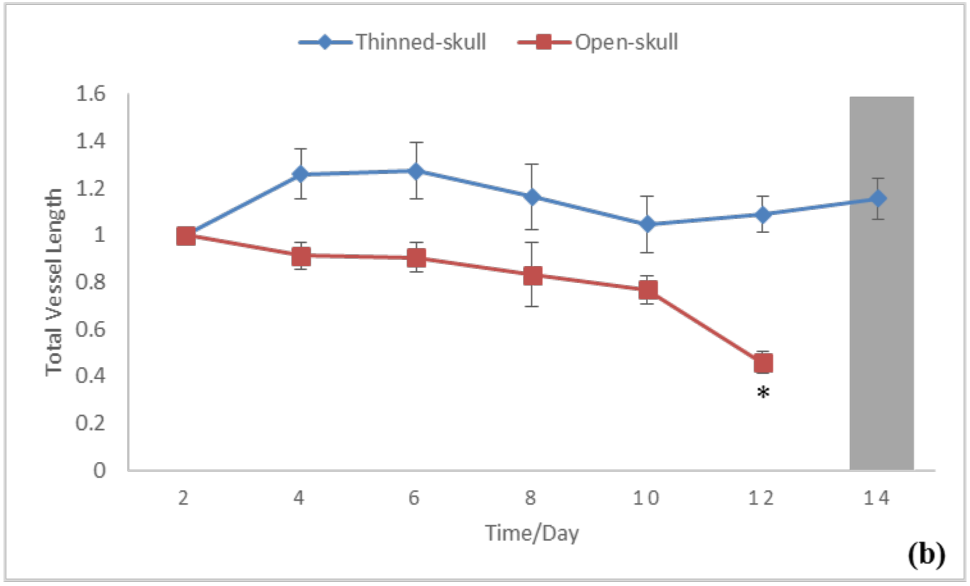

Figure 3.5 Trend in MVD (a) and total vessel length (b) between the thinned-skull and open-skull groups.

3.4 Discussion

The ‘n-shaped’ CNR curve for the thinned-skull group might result from a combination of the inflammatory response and skull regrowth. The first increase in CNR could be due to the window site recovering from the thinned-skull surgery, the CNR of day 6 was significantly higher than day 2. Also CBF in some surface vessels was disrupted because of the skull thinning procedure. The wound healing process led to an angiogenic response, as is evident from the significant increase in MVD from day 4 to 6. . An example of this is shown in **Fig 3.2** (blue arrows), which illustrates the development of the blood vessel from day 2 to 8. After day 6, both CNR and MVD began to decrease, which might be attributable to skull regrowth. An example of this is shown by comparing the ROI within the red boxes in **Fig 3.2** from day 8 to 12. The white, noisy features within the vessel region in **Fig 3.2** (red boxes) are indicative of skull regrowth, which leads to the decrease in CNR. Some vessels are unresolvable by LSCI due to skull regrowth, therefore resulting in a decrease in MVD as well. This observation has important ramifications for experiments in which detecting CBF changes could become obscured due to an increase in static scattering due to bone regrowth (after day 10). The open-skull (craniotomy) preparation was more invasive than the thinned-skull window. A possible explanation for the monotonic decrease in CNR and MVD is that the open-skull group was still in recovery phase during the fourteen day monitoring period.

Collectively, the observations in this study help answer the question of whether to employ a thinned-skull or open-skull preparation for in vivo laser speckle contrast imaging. The thinned-skull window requires a short recovery period (~ four days). Also, thinned-skull window provides a larger field of view than open-skull. It is challenging to perform a craniotomy with > 5 mm diameter window. The larger field of view of the thinned-skull window facilitates wide-field imaging of more distal regions of the cortex (e.g. middle cerebral artery) (Hecht, He et al. 2012), or whole brain imaging (Shaik, Kim et al. 2015). On the other hand, the open-skull window facilitates chronic or long-term in vivo imaging relative to the thinned-skull window. For example, LSCI was used to image vascular remodeling after ischemic stroke for thirty-five days using an open-skull window (Schrandt, Kazmi et al. 2015). However, the four to six week recovery period after window implantation might not be amenable to all experiment protocols.

In conclusion, we have systematically demonstrated that each window preparation has its own strengths and weakness and one must be cautious when selecting a window preparation based on the suitability of the experimental paradigm and the biological question being explored.

CHAPTER 4 MINIATURIZED OPTICAL NEUROIMAGING IN UNRESTRAINED ANIMALS

Another part of the thesis was to develop a multi-modal miniaturized head-mounted microscope, which could perform the same imaging modalities in the benchtop system (**Fig 2.2**) on awake, freely moving animals. Several advantages over the benchtop system can be appreciated. Without the confounding effect of anesthetics on CBF, normal physiological parameters of the brain could be obtained. Also, multiple animals could be monitored simultaneously with the miniaturized microscopes, and high-level functions such as social interactions of the mice could be studied. As a part of this project, we reviewed the current progress in miniaturized optical neuroimaging in unrestrained animals. With the permission of Elsevier, final published version of the manuscript is reformatted and attached to this thesis. The link to the publication on ScienceDirect is doi:10.1016/j.neuroimage.2015.02.070.

4.1 Abstract

The confluence of technological advances in optics, miniaturized electronic components and the availability of ever increasing and affordable computational power have ushered in a new era in functional neuroimaging, namely, an era in which neuroimaging of cortical function in unrestrained and unanesthetized rodents has become a reality. Traditional optical neuroimaging required animals to be anesthetized and restrained. This greatly limited the kinds of experiments that could be performed *in vivo*. Now one can assess blood flow and oxygenation changes resulting from functional activity and image functional response in

disease models such as stroke and seizure, and even conduct long-term imaging of tumor physiology, all without the confounding effects of anesthetics or animal restraints. These advances are shedding new light on mammalian brain organization and function, and helping to elucidate loss of this organization or 'dysfunction' in a wide array of central nervous system disease models.

In this review, we highlight recent advances in the fabrication, characterization and application of miniaturized head-mounted optical neuroimaging systems pioneered by innovative investigators from a wide array of disciplines. We broadly classify these systems into those based on exogenous contrast agents, such as single- and two-photon microscopy systems; and those based on endogenous contrast mechanisms, such as multispectral or laser speckle contrast imaging systems. Finally, we conclude with a discussion of the strengths and weaknesses of these approaches along with a perspective on the future of this exciting new frontier in neuroimaging.

4.2 Introduction

Imaging the brain has provided unprecedented insights into its functioning as well as disruption of this function due to various neuropathologies. Noninvasive imaging techniques such as functional Magnetic Resonance Imaging (fMRI) (Heeger and Ress 2002), Positron Emission Tomography (PET) (Nasrallah and Dubroff 2013) and Computed Tomography (CT) (Cianfoni, Colosimo et al. 2007) have been widely used for neuroimaging. However, these clinical or 'human-scale' imaging modalities often lack the resolution to spatially and temporally resolve underlying neuronal processes. Therefore, investigators circumvented this drawback by utilizing pre-clinical animal models in conjunction with imaging methods capable of high spatial and temporal resolution.

The availability of an ever-increasing spectrum of optical contrast agents (Zhang, Campbell et al. 2002), and technical advances in optics (Kerr and Denk 2008, Tye and Deisseroth 2012), coupled with optogenetic constructs for manipulating neuro-circuitry (Tye and Deisseroth 2012), have resulted in optical neuroimaging becoming the tool of choice for neuroscientific applications. Moreover, these optical neuroimaging techniques permit cellular-scale spatial resolution and millisecond temporal resolution (Kerr and Denk 2008).

Much of today's optical neuroimaging is performed using sophisticated optics and cumbersome electronic hardware (Theer, Hasan et al. 2003). The bulky nature of such setups requires the animal to be anesthetized and restrained stereotactically, greatly limiting the types of experiments that can be performed *in vivo* and at multiple time points. Additionally, the use of anesthetics has been found to alter the baseline physiology of the brain during *in vivo* imaging (Bonhomme, Boveroux et al. 2011). Therefore, miniaturization of the imaging hardware in conjunction with the ability to image the brains of awake and unanesthetized animals would circumvent these issues.

Recent advances in miniaturized optics and electronic devices (Theuwissen 2008) paved the way for the "next generation" optoelectronic systems capable of unique real-time, awake optical imaging. **Fig 4.1** shows the evolution of benchtop to 'head-mounted' neuroimaging systems. It is not always necessary to miniaturize the entire system. As shown in **Fig 4.1**, depending on the type of experiment, individual elements of the imaging system can be modified to match the required level of animal mobility. This can range from having the animal's head affixed while the animal pedals on a moving ball (Dombeck, Khabbaz et al. 2007), to systems that allow unrestrained animal mobility (Ghosh, Burns et al. 2011). It is worth noting that similar technical advances were also responsible for the development of 'implantable' microimagers (Ng, Tokuda et al. 2008). These implantable devices are image sensor array chips that have been packaged into 'ready-to-use' modules. Recent work has elegantly demonstrated their utility in applications ranging from neural imaging (Ng, Tamura et al. 2008) to blood-flow imaging in freely moving rats (Haruta, Kitsumoto et al. 2014). However, the focus of the current review is on non-implantable imagers. An excellent recent review by Kerr and Nimmerjahn focused on functional imaging at the cellular level and primarily covered imaging approaches that utilized exogenous contrast agents (Kerr and Nimmerjahn 2012). In this review, we examine miniaturized neuroimaging systems that utilize exogenous contrast agents, e.g. wide-field fluorescence imaging (Ferezou, Bolea et al. 2006, Flusberg, Nimmerjahn et al. 2008), two-photon fluorescence imaging (Helmchen, Fee et al. 2001, Sawinski, Wallace et al. 2009), as well as those that exploit intrinsic optical properties of biological tissues, e.g. multispectral imaging and blood flow based laser speckle imaging systems (Liu, Huang et al. 2013). Finally, we discuss the relative advantages and disadvantages of each approach and the exciting prospects of this technology from the micro- (i.e. cellular) to the macro-scale (i.e. whole tissue) for neuroimaging.

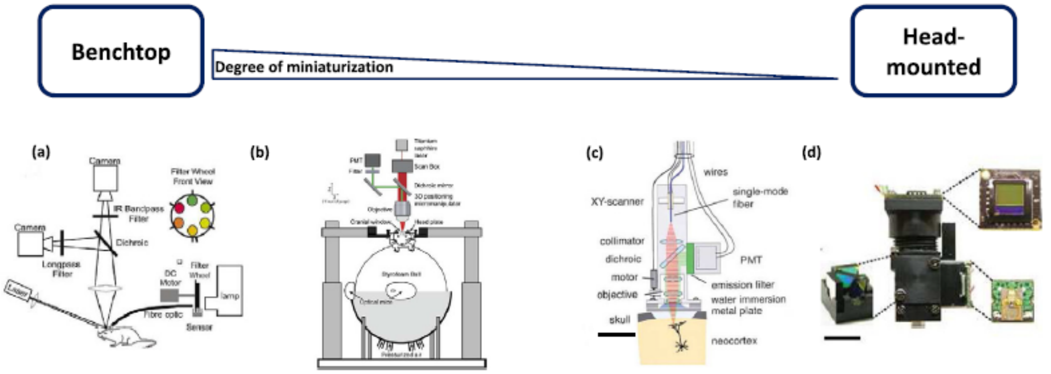

Figure 4.1 Evolution of benchtop to 'head-mounted' neuroimaging systems

The degree of miniaturization increases from (a to d). (a) A dual modality benchtop system for simultaneous multispectral imaging and laser speckle contrast imaging in anesthetized animals (Jones, Shin et al. 2008). (b) Schematic of the system setup for imaging in head-restrained, awake mice (Dombeck, Khabbaz et al. 2007). The head-mounted imaging system was modified from a standard two-photon microscope. The head of each mouse was restrained while the animal moved on a treadmill for behavioral testing. (c) Additionally miniaturized fiber-optics-based system (Helmchen, Fee et al. 2001), in which the photomultiplier tube (PMT) was incorporated into the head piece, wherein the excitation light source was still derived from a benchtop system. The head piece was 7.5 cm long (Scale bar = 23.5 mm). (d) An integrated head-mounted system (Ghosh, Burns et al. 2011), using surface mounted LEDs for exciation and a minaturized CMOS sensor for detection (Scale bar = 5 mm). This self-contained system enabled experiments involving interactive and natural behavioral tests. All images have been adapted with permission of the publishers.

4.3 Miniaturized optical systems based on exogenous contrast agents

Optical contrast agents permit visualization of underlying microvasculature

(Bassi, Fieramonti et al. 2011) as well as functional cellular dynamics such as membrane potentials (Mutoh, Perron et al. 2011) and intercellular calcium concentrations (Mittmann, Wallace et al. 2011). Conjugation of fluorescent dyes with genetically encoded biomarkers/target molecules (Chalfie, Tu et al. 1994), as well as their ability to shift emission spectra in response to biological perturbations (McVea, Mohajerani et al. 2012) has enabled fluorescent imaging to be utilized in a wide range of applications (Petersen, Grinvald et al. 2003, Mank, Santos et al. 2008). Although, variability in contrast agent delivery or unstable gene expression can affect the emitted fluorescence, an ever increasing array of fluorescent dyes with different excitation spectra, better quantum yields and extinction coefficients has greatly enhanced our ability to simultaneously monitor a multitude of targets and neurophysiologic processes.

Miniaturization of fluorescent microscopy was first attempted by using an optic fiber bundle to relay the emitted fluorescent light as well as the high intensity excitation illumination to and from a standard benchtop system (Helmchen, Fee et al. 2001). However, recent technological breakthroughs have enabled additional miniaturization of fluorescent microscopy systems as discussed below. A summary of miniaturized and mobile brain imaging platforms from the recent literature can be found in **Table 4.1**.

4.3.1 Single-Photon Microscopy Systems

Since single-photon microscopy does not need an expensive near-infrared laser and laser scanning mechanism, it is less complicated and more affordable than two-photon microscopy. These advantages also make it well-suited for miniaturized optical neuroimaging applications. The absence of a laser scanning mechanism endows single-photon microscopy with a high temporal resolution that is suitable for imaging dynamic neurobiological phenomena. However, single-photon systems can only acquire two dimensional images and the use of wide-field excitation increases the risk of photo-bleaching the sample.

Ferezou et al. were one of the first to report *in vivo* fluorescent imaging in freely moving animals (Ferezou, Bolea et al. 2006). In their system, a customized multi-fiber array (**Fig 4.2a**) placed in direct contact with the rat whisker barrel cortex relayed emission and excitation light to and from a standard benchtop epifluorescence imaging system. A voltage sensitive dye (RH1691) was employed for functional imaging of the barrel cortex following whisker stimulation. The dye primarily stained layer 2/3 sensory neurons. The system had a temporal resolution of 2 ms and covered a 3 mm × 3 mm field of view (FOV). Spatial resolution was limited by the size of individual fibers in the fiber optic bundle as well as by the low numerical aperture due to the absence of an objective lens at the specimen-optical fiber interface. While the exact spatial resolution of the system was not reported, the authors could successfully visualize the barrel cortex at sub-columnar resolution. Images from the fiber optic microscope were compared with those from a conventional fluorescent imaging setup, and no significant differences in peak fluorescence amplitude, duration or spatial extent of the sensory response to whisker stimulation were observed. Furthermore, the sensory response to whisker stimulation in rats anesthetized with isoflurane was compared to that of awake rats.

The authors showed that awake animals exhibited a response longer in duration and larger in spatial extent than their anesthetized counterparts (Ferezou, Bolea et al. 2006).

(Murayama, Perez-Garci et al. 2007) reported a single-photon fiber optic system for recording dendritic calcium signals (**Fig 4.2b**). To illuminate and collect light locally from the distal dendrites of cortical layer 5 neurons, an optic fiber was directly inserted into layer 5 of the rat's brain. To acquire different views of the dendrites, two optical setups were employed: the first included a one-fiber system for a side-on view; and the second was a two-fiber system for imaging above the cortex. The one-fiber system was tested on freely moving rats. After injecting a calcium-sensitive dye (Oregon Green 488 BAPTA-1), calcium signals were recorded from layer 5 neurons in stationary and free moving states, as well as during whisker stimulation. The amplitude of the calcium signals was observed to vary with the state of the animals. Furthermore, the authors simulated the effects of motion on their image acquisition by using a bench top stirrer assembly to vibrate an anesthetized rat while the microscope continuously acquired images. No significant changes were observed in the fluorescent signal from calcium transients. A later publication using the same system investigated dendritic calcium changes in layer 5 pyramidal cells of the somatosensory cortex in rats following sensory stimulation (Murayama, Perez-Garci et al. 2009). Their results showed that the strength of sensory stimulation was encoded in the calcium response of local layer 5 pyramidal cells in a graded manner.

(Flusberg, Nimmerjahn et al. 2008) reported a miniaturized singe-photon microscope for cellular-level imaging at frame rates up to 100 Hz. The optical components of the microscope consisted of a compact coupling assembly, focusing mechanism and two separate objective lenses. The head-mounted microscope weighed only 1.4 g and had a spatial footprint on the scale of a centimeter (**Fig 4.2c**). This ensured that the microscope could be easily supported by an adult mouse. The head piece was then connected to a standard benchtop fluorescent imaging system. The dual objective lenses ensured that both superficial and deep tissue could be imaged. Limitations in packing density and number of individual fibers in the optic fiber bundle restricted the lateral resolution and FOV to ~ 2.8-3.9 μm and ~ 240-370 μm, respectively. Its 75 Hz data acquisition rate made it possible to discern the movement of individual erythrocytes within blood vessels. Tests on freely moving mice revealed that motion artifacts were limited to less than 2 μm of lateral displacement. The microscope was used to record surface blood flow in the mouse neocortex and in the CA1 region of the hippocampus. Using temporal cross-correlation analysis, the authors demonstrated that blood flow velocities varied greatly among capillaries, venules and arterioles. The microscope was also used to compare Purkinje cell dendritic Ca^{2+} dynamics during the anesthetized and mobile states. Purkinje cells exhibited larger Ca^{2+} spike rates during locomotion than at rest. Additionally, correlation analysis of Ca^{2+} spiking between pairs of Purkinje cells revealed larger correlation coefficients during active movements than at rest.

(Cha, Paukert et al. 2014) designed a fiber-optic fluorescence microscope that used an objective focusing lens consisting of two symmetric aspheric lenses covering a ~4 mm^2 FOV. Their fiber optic bundle interfaced with a standard benchtop based fluorescence system. *In vitro* imaging demonstrated that this system was capable of resolving astrocytes and pyramidal cells in a mouse brain section, and image quality was comparable to that of a conventional fluorescence microscope. *In vivo* experiments with this system were conducted on head-restrained, awake mice placed on a treadmill. Using this microscope, the authors were able to demonstrate that Bergmann glia in the cerebellum showed larger amplitude of Ca^{2+} signals during locomotion than when the animal was at rest.

The ‘next-generation’ neuroimaging systems were fully miniaturized by using surface mount light emitting diodes (LEDs) for excitation illumination and minute (~3mm × 3mm) CMOS image sensors for image acquisition. These miniaturized microscopes enabled a transformation of the experimental paradigm from one in which restrained animals were imaged, to one in which interacting or naturally behaving animals could be imaged.

(Osman, Park et al. 2011, Park, Platisa et al. 2011, Osman, Park et al. 2012) designed a neuroimaging system with a miniaturized illumination source, focusing optics and image sensor (**Fig 4.2d**). This microscope featured a frame rate of 500 frames per second (fps) and a sensitivity of 0.1% of the initial fluorescent signal (0.1% $\Delta F/F$). Weighing 10 g, the system had a FOV of ~4.8 mm^2, lateral resolution of 25 μm and a 1.8 magnification ratio. Without a physical shutter, the system required very stable illumination to precisely control the exposure time.

Therefore, the LED output was actively controlled by a photodiode and microcontroller to maintain light intensity within 0.2 % deviation of its mean intensity. Small changes (< 1% ΔF/F) in barrel cortical fluorescence signals due to whisker stimulation were detectable using a voltage sensitive dye (RH1691). As reported in (Osman, Park et al. 2012), the resulting signal quality was comparable to that of a benchtop fluorescent microscope equipped with a Red-Shirt-Imaging camera (Decatur, GA). However, this microscope was not a fully miniaturized prototype. The image acquisition controller was a non-miniaturized field-programmable gate array (FPGA) assembly with an electric wire bundle connected to the head piece. The microscope's use is limited because the tether's rigidity could affect the animal's mobility in certain kinds of functional experiments.

(Ghosh, Burns et al. 2011) designed a similarly miniaturized fluorescence microscope (**Fig 4.2e**). Weighing only 1.9 g, it could be easily carried by an adult mouse. A maximum FOV of 600 × 800 μm was reported while supporting a magnification ratio of 5.0 and a lateral resolution of ~2.5 μm. The microscope was capable of high-speed cellular level imaging up to a frame rate of 100 Hz while covering a FOV of ~0.5 mm^2. Using this system, synaptic activation via calcium tracking in up to 206 Purkinje neurons from nine cerebellar microzones was reported. The microscope was first used to study the microcirculation during mobile and rest states of mice. The authors reported an increase in erythrocyte flow speeds when the animals transitioned from rest to locomotion states. Additional studies were focused on differentiating synaptic dynamics of freely moving mice during different behavioral states using a fluorescent calcium indicator. The authors showed that mean spike rates increased as the animal transitioned from rest to groom to locomotion states, respectively (Ghosh, Burns et al. 2011). When compared to the fiber-optic-based microscope previously reported by the same group (Flusberg, Nimmerjahn et al. 2008), the new microscope showed better performance in terms of optical resolution, fluorescence signal quality and system robustness. The FOV of the fiber-bundle-based microscope was restricted by the maximum diameter and bending radius of the bundle, while the FOV in this new microscope was only limited by sensor size and the focusing optics. Additionally, the fiber bundle microscope exhibited drastic attenuation of the transmitted fluorescent light due to bending and light absorption of the fiber. The fluorescence detected by the sensor increased from ~20% to 95% while a ~700% greater FOV was achieved. No realignment of the optics was necessary between imaging sessions, and the imaging duration could be extended up to 45 min. Observed motion artifacts were limited to less than 1 μm even when imaging running animals.

(O'Sullivan, Heitz et al. 2013) reported the fabrication of a miniature, integrated semiconductor-based fluorescence sensor, designed for detecting fluorophores and tumor-targeted molecular probes (**Fig 4.2f**). The system consists of multiple vertical-cavity surface-emitting laser (VCSEL) dies as the excitation source, whilst having two GaAs photodiodes functioning as two point detectors, and a CMOS (Complementary Metal Oxide Semiconductor) ROIC (Read-out Integrated Circuit) mounted on a custom printed circuit board (PCB). A standard 18-pin connector was employed for data transmission. The system was extremely light weight (~0.7 g) with a small footprint (~1 cm^3). VCSEL excitation wavelengths were optimized for the Cy 5.5 dye, and the emission filter was directly coated on to the custom-made image sensor. The onboard photocurrent ranged from 5 pA to 15 nA, was amplified and digitized using the ROIC for the observed light levels. When the system was tested on freely moving mice, the authors reported an increase of ~ 500 pA in the photocurrent following injection of Cy 5.5 fluorescence dye. This miniaturized system required precise positioning and fixation to the targeted object, which made it difficult to use on soft tissue or when imaging small targets (O'Sullivan, Heitz et al. 2013).

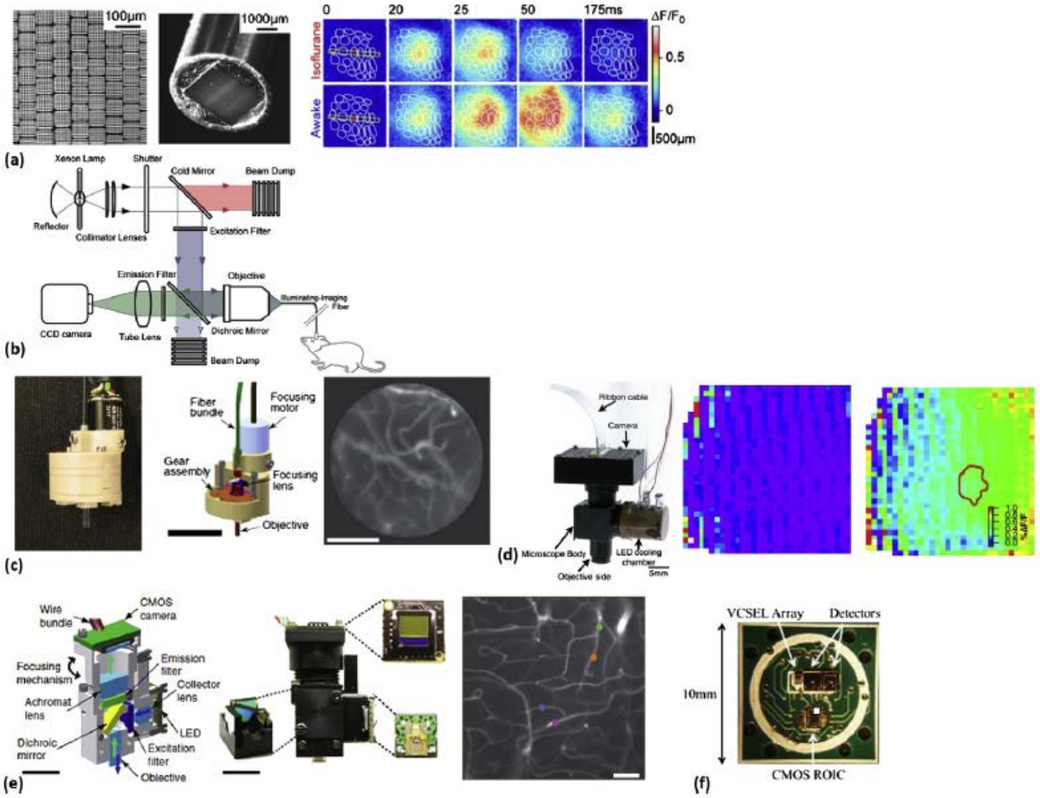

Figure 4.2 Miniaturized single-photon optical systems

(a) Images of the custom manufactured fiber optic bundle from (Ferezou, Bolea et al. 2006), based on wound image bundle technology (Schott Fiber Optics, Southbridge MA). The left panel shows a high-maginification image of the fiber bundle tips: each group consisted of 6×6 fibers; each fiber had 8 μm cores and a resulting numerical aperture of 0.6. The middle panel shows an image of the fiber bundle (diameter ~ 5mm) that was in direct contact with rat cortex. The right panel shows the comparison of cortical responses to C2 whisker purtabation imaged by VSD between isoflurane anesthetized and awake mouse. VSD analysis on C2 barrel column revealed that the duration of response was much longer in awake mouse. (b) Single-fiber system schematic for side-on imaging of pyramidal cells in layer 5 of the rat neocortex (Murayama, Perez-Garci et al. 2007). The fiber bundle was used to transmit exciation light and collect fluorescence signals from a standard benchtop system. (c) Fiber optic single-photon microscope from (Flusberg, Nimmerjahn et al. 2008), showing the head mount comprising of focusing optics, the fiber bundle and focusing motor. The head piece weighed 1.1 g, and the system had a frame rate of less than 100 Hz. The two GRIN objective lenses of different focal lengths enabled deep (6.2mm) and superficial tissue (1.4mm) imaging. The right panel shows the image of neocortical vasculature from an awake freely moving mouse (Scale bar = 100 μm). (d) A self-contained fluorescence microscope (Osman, Park et al. 2012), consisting of a LED light source, CMOS image sensor, focusing optics and exciatation/emission filters. The microscope was aimed at high speed imaging and detecting small changes (< 1% ΔF/F) in fluorescence signals. The middle panel shows a baseline %ΔF/F image of mouse barrel cortex stained with VSD RH1691 (averaged from 9-12 ms before whisker deflection). The right panel shows an average %ΔF/F image in the same FOV 9-12 ms after the onset of stimulation (Osman, Park et al. 2012). (e) Self-contained one-photon microscope (Ghosh, Burns et al. 2011), light source (LED) and image sensor (CMOS camera) were mounted on the head piece (weight ~ 1.9g). The electrical signal was transmitted via the wire bundle to a FPGA, for both LED control and image acquistion. Microvasculature of freely behaving mouse was acquired after injection of fluorescein-dextran. The image is the standard deviation from 10 second acquisition, to emphasize vasculature. (Scale bar = 50 μm) (f) Photograph of the VCSEL-CMOS sensor reported by (O'Sullivan, Heitz et al. 2013). The custom PCB with bonded chips, consists of multiple VCSEL excitation sources, two GaAs photodiodes and a CMOS read-out integrated circuit (ROIC). All images have been adapted with permission of the publishers.

4.3.2 Two-Photon Microscopy Systems

Two-photon microscopy (2PM) uses ultra-short pulses of a long wavelength laser to scan biological tissue in three dimensional space, creating a depth resolved image stack. This approach excites only the voxel being imaged, thereby minimizing photo-toxicity. Additionally, the use of a longer wavelength excitation light reduces scattering in biological tissues, enabling deeper imaging depths. Nonetheless, laser scanning impacts the acquisition frame rate, enabling only relative slow phenomena to be imaged. Also, the laser scanning pattern can be distorted by the motion of awake, unrestrained animals. Due to the high power and temporal modulation accuracy required of the laser, miniaturized 2PM systems utilize a standard benchtop 2PM system retrofitted with an optical fiber bundle, and focusing optics to deliver excitation and collect the emitted light from the freely moving animal.

Helmechen et al. reported the first miniaturized head-mounted two photon microscope (Helmchen, Fee et al. 2001). The head piece consists of a single-mode optical fiber for excitation, a miniature scanning device, microscope optics and a miniature photo multiplier tube (PMT) (**Fig 4.3a**). Two-dimensional scanning was realized by resonant scanning in a Lissajous pattern. A line scanning mode was also available for faster imaging. The microscope was 7.5 cm long, 25 g in weight and could be supported by an adult rat. *In vivo* imaging on anesthetized rats injected with a dextran dye showed surface blood vessels and the underlying capillary network. The maximum imaging depth was 250 μm. Furthermore, imaging on anesthetized rats injected with a calcium indicator (calcium green-1) resolved dendritic processes in layer 2/3 neurons. Testing this microscope on freely moving animals, the authors determined that rapid turning of the head and sudden contact with a wall induced noticeable motion artifacts in the acquired fluorescence images.

A two-photon microscope with two objective gradient-index(GRIN) lenses for miniaturized focusing was built by (Gobel, Kerr et al. 2004). Pre-compensation for the broadening of excitation light within the optic fiber was achieved by pre-chirping the laser pulses. Lateral and axial resolutions of 2.5 μm and 20 μm, respectively, were achieved. The pixelated image was smoothed with a Gaussian filter to compensate for the 1 μm spacing between individual fibers in the optic fiber bundle, which also reduced image contrast. As proof of concept for the device, *in vivo* imaging of fluorescein-injected, anesthetized rats was performed to visualize blood vessels.

(Piyawattanametha, Cocker et al. 2009) reported a portable 2PM microscope based on a microelectromechanical systems (MEMS) laser scanning mirror (**Fig 4.3b**). The system weighed 2.9 g. Moreover, the implantation of the MEMS scanner made the 2PM system more compact, i.e. 2 cm×1.9 cm×1.1 cm in size. Separate optical fibers for fluorescence collection and excitation pulse delivery were utilized. The system had transverse and axial resolutions of 1.29±0.05 μm and 10.3±0.3 μm, respectively, with a maximum FOV of 295×100 μm and was used to image neocortical capillaries in mice injected with fluorescein dye. In the line scanning mode, individual erythrocytes inside blood vessels could be tracked in an anesthetized animal.

(Sawinski, Wallace et al. 2009) reported a miniaturized head-mounted 2PM system for recording Ca^{2+} transients from the somata of layer 2/3 neurons in the visual cortex of awake, freely moving rats (**Fig 4.3c**). As described by the authors, 'a custom designed water-immersion lens and a leveraged non-resonant fiber scanner were employed, providing greater control over the scan pattern than resonant scanning' (Sawinski, Wallace et al. 2009). Their multi-lens setup provided higher excitation and detection numerical apertures (NA) compared to using a single GRIN lens. Besides neuronal activity resulting from visual stimuli, bending of the optical fiber also caused fluctuations in the detected fluorescence signals. To counteract this, two fluorescent dyes, a green calcium indicator (Oregon green BAPTA-1, OGB1) and sulforhodamine 101 (SR101) were employed. Since SR101 fluorescence was not related to neuronal activity, it was used to normalize the signal from the green fluorescent calcium indicator. They conducted one of the first *in vivo* experiments on freely moving animals on a semicircular track. They placed three monitors with different visual stimuli at the apex and the ends of the track. The experiment was conducted in the dark except for light stimulation from the monitors. Synchronized infrared videos were recorded during the experiment to investigate the relationship between animal movement and calcium indicator signals. A significant increase in calcium transients was observed when the animal swept its gaze across the visual stimuli. It should be noted that motion artifacts were observed during chewing and head movement of the animals. Of these, lateral displacements were corrected by an automated algorithm as described in (Greenberg and Kerr 2009).

(Barretto, Messerschmidt et al. 2009) designed a micro-lens-based 2PM imager. By combing a GRIN lens with a plano-convex lens, their set-up was corrected for aberration and had a higher numerical aperture than just using the GRIN lens by itself. In vivo images of GFP-expressing pyramidal cells in region CA1 of the mouse hippocampus showed better resolution than images acquired using the GRIN lens alone. Finally, Helmchen et al. provide a detailed protocol for investigators interested in designing their own bespoke two-photon microscopy based systems for in vivo imaging in freely moving animals in (Helmchen, Denk et al. 2013). The dissemination of such hardware 'recipes' using commercially available components should make imaging in awake animals more widespread.

The feasibility of other approaches, such as diffuse optical tomography (Holzer, Schmitz et al. 2006), light-sheet-based microscopy (Engelbrecht, Voigt et al. 2010) and two-photon microendoscopes (Flusberg, Lung et al. 2005, Saunter, Semprini et al. 2012) has also been demonstrated in freely moving animals. Besides the abovementioned applications, head-mounted microscopes have also been used for studying cortical calcium waves in newborn mice (Adelsberger, Garaschuk et al. 2005), and for imaging hippocampal cells during virtual navigation tasks (Dombeck, Khabbaz et al. 2007, Dombeck, Harvey et al. 2010).

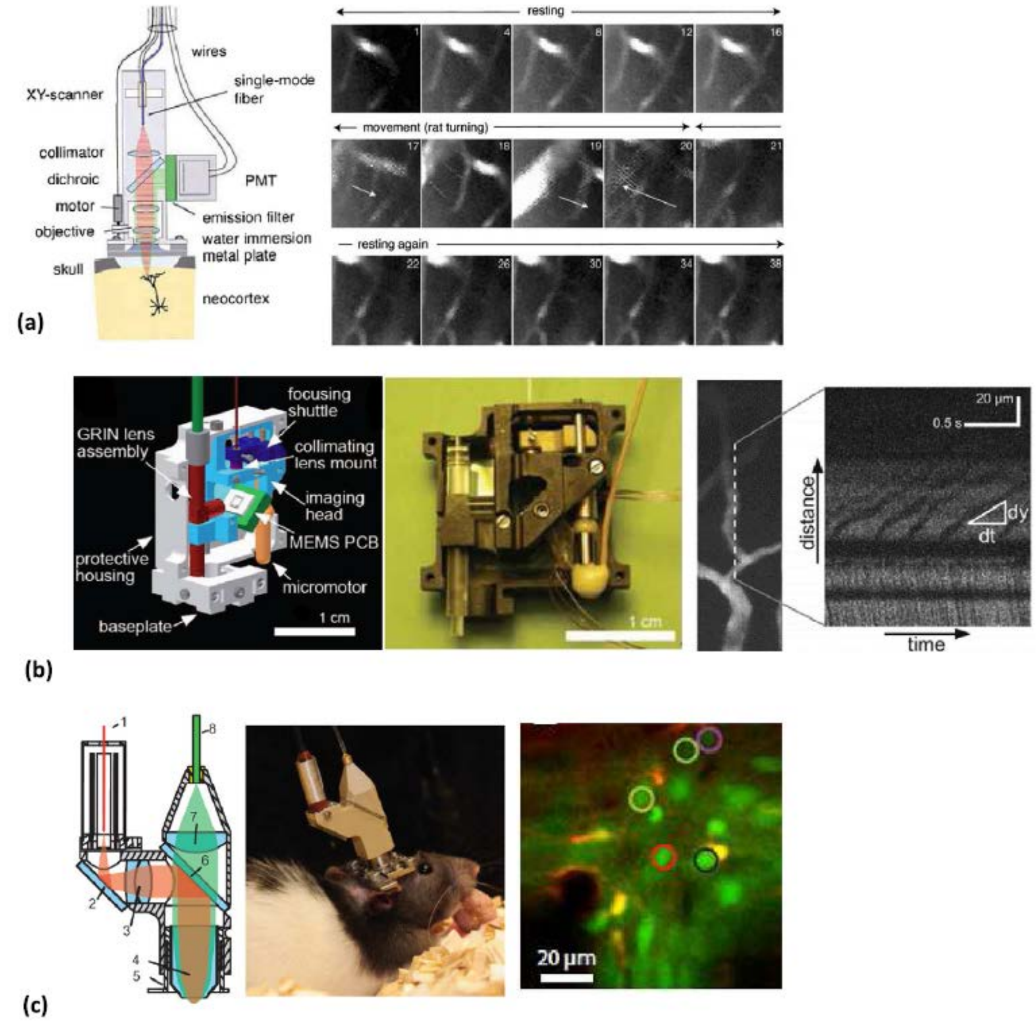

Figure 4.3 Miniaturized two-photon optical systems

(a) Left: The first reported head-mounted two-photon microscope (Helmchen, Fee et al. 2001). Near infrared laser excitation was coupled to a single mode fiber, collimated and focused by a water-immersion objective to the neocortex. Fluorescence signal collection was achieved by a PMT. Right: Sample images from an awake rat labeled with fluorescence dextran (0.5 s frame duration). Motion caused the FOV to shift from frame 17 to 20 (indicated by white arrows). (b) Schematic (left) and photograph (middle) of the two-photon microscope based on a MEMS scanning mirror (Piyawattanametha, Cocker et al. 2009), the microscope weighed 2.9 g, excitation pulse and fluorescence collection were separated by using two different types of optic fibers, which enhanced the SNR of the detected fluorescence signals. Right: Images of neocortical capillaries from an anesthetized adult mouse injected with fluorescein isothiocyanate-dextran dye. Line scanning mode (shown in d) allowed the microscope to track individual erythrocytes that flow was parallel with the line scanning. (c) Left: Schematic of the two-photon microscope, made up of: 1. single-mode excitation fiber; 2 folding mirror; 3, tube lens; 4, objective; 5, focusing flange; 6, beam splitter; 7, collimation lens; 8, multi-mode collection fiber. Middle: Photograph of a rat with the head-mounted microscope (Sawinski, Wallace et al. 2009); Right: Overlay of *in vivo* images acquired using two fluorescent dyes: SRS 101 that labels astrocytes (red channel) and the calcium indicator OGB-1 that labels neurons (green channel), from a rat's visual cortex. The colored circles indicate the neurons and the astrocyte from which signals were analyzed in response to visual stimulation.

4.4 Miniaturized optical systems based on endogenous contrast

The earliest form of intrinsic contrast based optical imaging was performed using multispectral imaging, which exploits the spectral properties of oxygenated and deoxygenated hemoglobin to visualize the relative oxygen saturation in biological tissue (Hillman 2007). Recently, laser speckle contrast imaging (LSCI), that relies on flowing blood for image contrast (Rege, Thakor et al. 2012), has also been miniaturized for freely moving animal experiments (**Table 4.1**).

4.4.1 Multispectral Imaging System

Multispectral imaging has a long and established history in neuroscience (Ts'o, Frostig et al. 1990). However, it lacks complementary contrast from other tissue structures because it does not rely on any exogenous contrast agents, but rather on the spectrally dependent absorption properties of hemoglobin moieties (Murari, Li et al. 2007). Nonetheless, miniaturized multispectral imaging provides a convenient way to observe tissue oxygenation changes in the brain.

(Murari, Greenwald et al. 2009) (Murari, Etienne-Cummings et al. 2010) designed a microscope with the potential for multi-modality neuroimaging. This system occupied ~4 cm^3 and weighed 5.4 g. A custom-made CMOS camera (15fps) was incorporated in the system. Cortical blood vessels 15-20 µm diameter could be visualized using this system. *In vivo* experiments on rats using a green LED light source demonstrated a reflectance change between the active state and rest state. Tests on fluorescence, LSCI and multispectral imaging, demonstrated the feasibility of developing a multi-modality miniaturized microscope for neuroimaging applications.

4.4.2 Laser Speckle Contrast Imaging System

Laser Speckle Contrast Imaging (LSCI) relies on the statistical properties of laser light scattered by red blood cells (RBCs) moving inside perfused blood vessels. A high blood flow velocity generates greater optical scatter and low speckle contrast and vice versa, this mechanism enables LSCI to assess relative blood flow changes as well as delineate microvascular structure from background tissue with a high contrast-to-noise ratio (Senarathna, Rege et al. 2013). However, LSCI typically requires an image stack to compute relative blood flow maps, thereby limiting its intrinsic temporal resolution.

(Miao, Lu et al. 2011) designed a head-mounted microscope for laser speckle contrast imaging (**Fig 4.4**). The microscope was ~20 g in weight and 3.1 cm height. This head-mounted system consisted of a miniature macrolens system, image sensor, optical fiber bundle and circuits. The spatial resolution achievable was 16 lp/mm with less than 2% distortion. To eliminate motion artifacts, registered laser speckle contrast analysis (rLASCA) was applied to the raw speckle data, wherein each image from the image stack was aligned with the first image. While the rat was free moving, blood vessels approximately 4 pixels or ~50 μm in diameter could be identified (**Fig 4.4**). This spatial resolution was comparable to that of standard benchtop laser speckle imaging systems and suitable for studying the cerebral blood flow (CBF) of major vessels under different physiological conditions (Miao, Lu et al. 2011). (Liu, Huang et al. 2013) designed a dual-modality LSCI/multispectral microscope, also extendable for fluorescence imaging (**Fig 4.4b**). The multi-modal microscope weighed 1.5 g, and the internal optical components were adjustable, providing different magnification ratios and FOVs. They conducted an extensive study on cortical spreading depression (CSD) in freely moving and anesthetized animals. Hemodynamic parameters were calculated from simultaneously acquired LSCI and dual-wavelength multispectral imaging data. The authors demonstrated that there was a significant difference in CSD propagation latencies between anesthetized and awake animals (**Fig 4.4b**). CSD in isoflurane-anesthetized rats was significantly longer in duration, and agreed with previous studies demonstrating that anesthetics extend CSD duration and reduce CSD frequency (Kudo, Nozari et al. 2008). Senarathna et al. (Senarathna, Murari et al. 2011, Senarathna, Murari et al. 2012) reported the development of a miniaturized LSCI microscope weighing 7 g and occupying less than 5 cm^3 (**Fig 4.4c**). The system consisted of a laser diode (tri-wavelength), focusing optics, CMOS sensor, with control circuits housed in a backpack. The tetherless setup made the microscope suitable for behavioral tests in freely moving rodents. LSCI images could be computed following acquisition of 240 raw speckle images. By converting speckle contrast to the correlation time of blood flow (Duncan and Kirkpatrick 2008), relative CBF maps were generated (**Fig 4.4c**). As reported in (Senarathna, Murari et al. 2012), the image quality degraded an hour after implantation. The authors concluded that this might be attributable to the refractive index matching material (i.e. mineral oil) gradually evaporating and the thinned skull optical window preparation eventually drying out. Also the use of a rolling shutter technique for exposure time control together with a relatively low frame rate of ~ 6 fps, resulted in long exposure times that averaged out some of the speckle contrast. The spatial resolution of the system was 20 μm which was the pixel size of the image sensor. Higher spatial resolution could be achieved by replacing it with a smaller pixel size CMOS sensor.

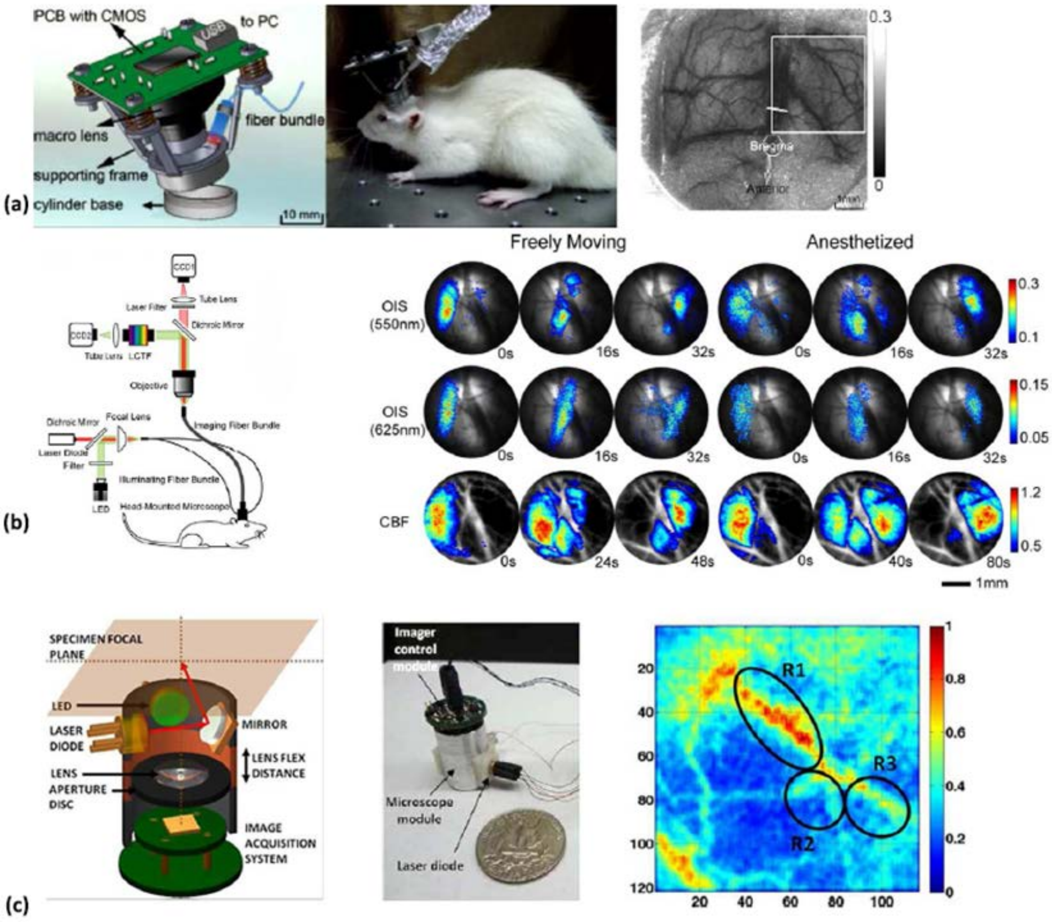

Figure 4.4 Miniaturized optical systems that utilize endogenous contrast agents

(a) Left: Schematic of a fiber-optics-based laser speckle imaging microscope. The illumination was fiber-coupled from a benchtop laser source and the camera chip was incorporated within the head piece. Middle: A rat with the head-mounted microscope that was ~ 20 g in weight and 3.1 cm in height. Right: *In vivo* laser speckle contrast image from a freely moving rat after co-registration analysis (Miao, Lu et al. 2011). The image shows the vascular network in the rat cortex over a 7mm × 7mm FOV. (b) Left: Schematic of dual-modal fiber-optic-based microscope designed by (Liu, Huang et al. 2013). The system consisted of three parts, a fiber-coupled dual illumination source, a head-mounted microscope and two CCD cameras system for dual modality acquisition. Right: Spatio-temporal distribution of hemodynamic changes from a cortical spreading depression (CSD) model illustrating the difference between anesthetized and awake states (Liu, Huang et al. 2013). (c) Schematic (left) and photograph (middle) of a self-contained laser speckle imaging microscope in which light from a VCSEL is reflected by a side mirror to accommodate different focal planes. The speckle signals were focused onto a custom made CMOS sensor by a single lens (Senarathna, Murari et al. 2012). Right: Relative blood flow map derived from speckle contrast images acquired using the microscope (laser wavelength λ = 795 nm) from the rat cortex over a ~1.85 mm × 2 mm FOV. The higher blood flow velocity of R1 indicates that R2 and R3 are downstream of R1 and that blood flow from R1 is branching off into R2 and R3.

4.5 Discussion

Miniaturized brain imaging systems, while having the advantages of portability, size, and multimodality neuroimaging in awake/unrestrained animals are prone to several shortcomings. Therefore, the decision to utilize such an imaging system instead of a benchtop setup should be based on a balance of its strengths and weaknesses.

A major concern with miniaturized neuroimaging systems is the additional weight it imposes on the animal. While a benchtop system tethered to an animal via an optical fiber bundle imposes minimal additional weight, a fully miniaturized system requires the entire weight of the imaging system be borne by the animal. Hence, it is vital that such imaging systems are designed with critical weight limits for the applications under consideration. A similar argument applies to the spatial footprint of the device attached to the animal's head, including the total height and size of the instrumentation. Use of a larger species of animals, e.g. rats versus mice, might partially obviate this concern. Nonetheless, it is crucial that experimental protocols involving miniaturized, head-mounted microscopes clearly establish that the animal behavior under study is not significantly affected by the implanted or mounted neuroimaging system (Sawinski, Wallace et al. 2009).

Increased motion artifacts are another concern with studies in freely moving, unanesthetized animals. Beyond respiration and cardiac motion artifacts that are seen in benchtop imaging, miniaturized imaging platforms are susceptible to motion caused by whole-body movement as well as relative motion between the head-mounted microscope and the animal's body. Some imaging modalities are more sensitive to motion than others, e.g. 2PM suffers more from motion artifacts than wide-field fluorescence microscopy. Different image registration and motion removal algorithms can be employed to enhance image quality (Dombeck, Graziano et al. 2009).

Another important aspect of imaging in awake, freely moving animals is the interpretation of animal behaviors correlated with neural responses. Different types of monitoring tools have been employed to monitor animal activities for various applications. Typically, synchronized videos are recorded during experiments to document the animal's activities. In (Sawinski, Wallace et al. 2009), the positions of four infrared LEDs attached to the microscope were used to determine animal's movement and orientation of its head. By classifying the animal's behavior with respect to the monitors displaying visual stimuli, the relationship between visual perturbations and simultaneous recorded calcium signals could be studied. In (Dombeck, Khabbaz et al. 2007), running speeds were measured by the rotation of a spherical treadmill and infrared videos were recorded to observe grooming and whisking. The relationship between fluorescence signal changes from behavior and running traces were analyzed, a significant fraction of neurons showed strong running correlation. As reported by the authors, transients of some the neurons exactly mimicked the time course of running speed.

A frequently overlooked aspect of miniaturized imaging systems is the challenge of building them from high-performance optical and electronic components in view of their size, weight and power constraints. Therefore, due to limitations in current hardware and optical component fabrication, compact imaging systems usually offer ‘bare-bones’ imaging capabilities that are customized to a given experimental paradigm. In doing so, such systems lack the imaging precision, accuracy and flexibility of conventional benchtop systems. For example, in miniaturized LSCI systems, the VCSEL laser source may emit laser light that is not perfectly coherent, thereby degrading speckle contrast. While a benchtop setup can be easily focused, the magnification changed and multiple wavelengths used simultaneously, a miniaturized neuroimaging system has limited focusing ability and usually has one fixed magnification level and one needs to image different wavelengths sequentially. Therefore, flexibility and precision need to be considered before choosing a miniaturized neuroimaging system over a conventional benchtop imaging system.

4.6 Conclusions and future directions

In the past decade, traditional benchtop based microscopy of anesthetized and constrained animals has slowly made way to neuroimaging in freely moving animals. Technological innovations in electronic hardware, miniaturized optics and computing power have converged to make this tremendous advance possible. This has brought about a paradigm shift in neuroscience, enabling scientific investigations geared towards uncovering natural brain function and dysfunction due to disease. Since optical imaging is relatively simple to operate in contrast to other imaging modalities such as ultrasound, MRI etc., the construction of miniaturized neuroimaging platforms has experienced an exponential growth (**Table 4.1**).

Early instrumentation for brain imaging in freely moving animals involved a standard benchtop microscope coupled to an optical fiber bundle that attached to an optical window over the animal's intact brain. The next generation of neuroimaging systems utilized optics inserted in to the animal's head-mount, while keeping the rest of the microscope assembly unchanged. However, in the latest generation of neuroimaging systems, the development of miniaturized light sources and sensitive CMOS image sensors within the head-mounted microscope is making the need for optical fiber bundles less critical. Nonetheless, such imaging systems still require wires to connect the head-mounted instrumentation with advanced control circuitry on the benchtop, thus tethering the animal. Fully compact microscope systems that utilize miniature control and storage electronics encased in a backpack worn by the animal have begun to emerge, enabling truly tetherless animal brain imaging. With impending improvements in electronic and optical design, supported by the availability of sophisticated computer aided design (CAD) and rapid prototyping tools, fully mobile and ultra-compact head mounted systems can be envisioned. These will increase user convenience and make possible a range of experiments that were previously unfeasible due to the presence of tethers. Examples include behavioral experiments involving complex maze structures as well as group studies wherein brain function of multiple freely interacting animals can be simultaneously tracked as an ensemble.

While in their simplest form many head mounted optical microscopes have utilized a single imaging modality, integrated systems with two imaging modalities have begun to emerge. Most commonly, multispectral imaging, given its relative simplicity in implementation, is combined with another modality such as fluorescent or speckle imaging (Murari, Etienne-Cummings et al. 2010, Liu, Huang et al. 2013). Such systems provide scientists access to a multitude of biological variables enabling them to obtain a more holistic view of the neurobiology of awake and freely moving animals. Moving forward, given the need for acquiring multi-parametric data, the development of miniaturized systems with more than two imaging modalities may become commonplace.

Combining optical imaging with other neurobiological data such as electrophysiology (Szuts, Fadeyev et al. 2011), biochemical recordings etc., could lead to a multimodality system for studying the brains of freely moving animals. For example, visualizing cellular calcium dynamics with fluorescent imaging while simultaneously monitoring electrophysiology with a transparent electrocorticographic (ECoG) sensor array (Ledochowitsch, Olivero et al. 2011), could herald a new era of neurobiological investigation. Or one could envision experiments involving functional neuromodulation via electrical or optogenetic stimulation to assess interactions between stimulation and neuroimaging.

Future applications of miniaturized microscopes need not be limited to conventional neuroscience applications, but could include imaging in a wide array of preclinical disease models. For example, one could envisage the use of head mounted optical microscopes for ‘life-time’ imaging of brain tumor progression, or sudden onset/termination of seizures; imaging of neurovascular coupling, imaging neural plasticity or continuous imaging of the etiology of stroke. In summary, miniaturized optical head-mounted imaging systems have progressed considerably from their benchtop antecedents. We envision a future in which the use of such portable, user-friendly systems will become commonplace in neuroscience laboratories alongside advances in optogenetics and high-throughput electrophysiology. It is our belief that miniaturized optical neuroimaging in unrestrained animals will be a critical ingredient of the next-wave of breakthroughs in the neurosciences and investigations of brain-related pathologies.

Table 4.1 Summary of miniaturized and mobile brain imaging platforms

N/A = Microscope specifications were ‘not available’ in the referenced publication

Single-photon exogenous contrast microscopes:							
Contrast Agent	*Weight*	*Size*	*Field of View*	*In-plane Resolution*	*Temporal Resolution*	*Application*	*Reference*
VSD (RH1691)	N/A	N/A	3 × 3 mm^2	N/A	2 ms per frame	Whisker barrel cortex imaging	(Ferezou, Bolea et al. 2006)
Fluorescein-dextran, Ca^{2+} indicator (Oregon green)	1.1 g	N/A	0.07 mm^2	~ 2.8-3.9 µm	Up to 100Hz	Blood flow speed/distribution, Ca^{2+} dynamics of Purkinje cells	(Flusberg, Nimmerjahn et al. 2008)
GCaMP3	N/A	N/A	4 mm^2	N/A	N/A	Ca^{2+} imaging of Glia cells	(Cha, Paukert et al. 2014)
VSD (RH1692)	10 g	N/A	4.88 mm^2	25 µm	Up to 900 Hz	Whisker barrel cortex imaging	(Osman, Park et al. 2012)
Fluorescein-dextran, Ca^{2+} indicator (Oregon green)	1.9 g	N/A	~ 0.5 mm^2	~ 2.5 µm	36Hz or 100Hz	Blood flow speed/distribution, Ca^{2+} dynamics of Purkinje cells	(Ghosh, Burns et al. 2011)
Cy 5.5 dye	0.7 g	1 cm^3	N/A	N/A	N/A	N/A	(O'Sullivan, Heitz et al. 2013)
Two-photon exogenous contrast microscopes:							
Contrast Agent	*Weight*	*Size*	*Field of View*	*Lateral Resolution*	*Temporal Resolution*	*Application*	*Reference*
Fluorescent-dextran Ca^{2+} indicator (green-1)	25 g	7.5 cm long	N/A	Dendritic spines resolved	N/A	N/A	(Helmchen, Fee et al. 2001)
Fluorescein-dextran Rhodamine	N/A	N/A	0.8 mm diameter	Lateral: 2.5 µm Axial: 20 µm	N/A	N/A	(Gobel, Kerr et al. 2004)
Fluorescein-dextran	2.9 g	2×1.9×1.1 cm^3	N/A	Lateral: 1.29±0.05 µm Axial: 10.3±0.3 µm	1-15Hz	Blood flow analysis	(Piyawattanametha, Cocker et al. 2009)
GAD67-GFP	~ 1.5 g	N/A	300 µm diameter	Lateral: 3.2±0.4 µm Axial 5.1±1 µm	N/A	N/A	(Engelbrecht, Voigt et al. 2010)
Sulforhodamine 101 & Ca^{2+} indicator	5.5 g	N/A	N/A	Single soma resolved	90 ms per frame	Ca^{2+} dynamics from visual stimuli	(Sawinski, Wallace et al. 2009)
Calcium indicator	0.6 g	N/A	Up to 200 µm	Lateral: 0.98±0.09 µm Axial: 7.68±1.3 µm	25 Hz	Ca^{2+} dynamics of Purkinje cells	(Engelbrecht, Johnston et al. 2008)
Endogenous contrast microscopes:							
Contrast Agent	*Weight*	*Size*	*Field of View*	*Lateral Resolution*	*Temporal Resolution*	*Application*	*Reference*
LSCI	~ 20 g	3.1 cm long	N/A	16 lp/mm	N/A	Vasculature/relative blood flow	(Miao, Lu et al. 2011)
LSCI & Multispectral	1.5 g	N/A	N/A	5.5 µm	N/A	Cortical spreading depression	(Liu, Huang et al. 2013)
LSCI	~ 7 g	5 cm^3	3.5×3.3 mm	N/A	6 Hz	Vasculature/relative blood flow	(Senarathna, Murari et al. 2012)

BIBLIOGRAPHY

Adelsberger, H., O. Garaschuk and A. Konnerth (2005). "Cortical calcium waves in resting newborn mice." Nature Neuroscience **8**(8): 988-990.

Barretto, R. P., B. Messerschmidt and M. J. Schnitzer (2009). "In vivo fluorescence imaging with high-resolution microlenses." Nature Methods **6**(7): 511-512.

Bassi, A., L. Fieramonti, C. D'Andrea, M. Mione and G. Valentini (2011). "In vivo label-free three-dimensional imaging of zebrafish vasculature with optical projection tomography." Journal Biomedical Optics **16**(10): 100502.

Boas, D. A. and A. K. Dunn (2010). "Laser speckle contrast imaging in biomedical optics." Journal Biomedical Optics **15**(1): 011109.

Bonhomme, V., P. Boveroux, P. Hans, J. F. Brichant, A. Vanhaudenhuyse, M. Boly and S. Laureys (2011). "Influence of anesthesia on cerebral blood flow, cerebral metabolic rate, and brain functional connectivity." Current Opinion in Anaesthesiology **24**(5): 474-479.

Bray, R. C., K. R. Forrester, J. Reed, C. Leonard and J. Tulip (2006). "Endoscopic laser speckle imaging of tissue blood flow: applications in the human knee." Journal of Orthopaedic Research **24**(8): 1650-1659.

Briers, J. D. and A. F. Fercher (1982). "Retinal blood-flow visualization by means of laser speckle photography." Investigative Ophthalmology & Visual Science **22**(2): 255-259.

Briers, J. D. and S. Webster (1996). "Laser speckle contrast analysis (LASCA): a nonscanning, full-field technique for monitoring capillary blood flow." Journal Biomedical Optics **1**(2): 174-179.

Burster, T., H. Macmillan, T. Hou, B. O. Boehm and E. D. Mellins (2010). "Cathepsin G: roles in antigen presentation and beyond." Molecular Immunology **47**(4): 658-665.

Carpentier, G., M. Martinelli, J. Courty and I. Cascone (2012). Angiogenesis analyzer for ImageJ. 4th ImageJ User and Developer Conference proceedings.

Cha, J., M. Paukert, D. E. Bergles and J. U. Kang (2014). Fiber optic fluorescence microscopy for functional brain imaging in awake mobile mice. SPIE BiOS, International Society for Optics and Photonics.

Chalfie, M., Y. Tu, G. Euskirchen, W. W. Ward and D. C. Prasher (1994). "Green Fluorescent Protein as a Marker for Gene-Expression." Science **263**(5148): 802-805.

Cheng, H. and T. Q. Duong (2007). "Simplified laser-speckle-imaging analysis method and its application to retinal blood flow imaging." Optics Letters **32**(15): 2188-2190.

Cheng, H., Q. Luo, S. Zeng, S. Chen, J. Cen and H. Gong (2003). "Modified laser speckle imaging method with improved spatial resolution." Journal of Biomedical Optics **8**(3): 559-564.

Cianfoni, A., C. Colosimo, M. Basile, M. Wintermark and L. Bonomo (2007). "Brain perfusion CT: principles, technique and clinical applications." Radiologica Medica **112**(8): 1225-1243.

Davi, G. and C. Patrono (2007). "Platelet activation and atherothrombosis." New England Journal of Medicine **357**(24): 2482-2494.

Davis, S. M. and G. A. Donnan (2009). "4.5 hours: the new time window for tissue plasminogen activator in stroke." Stroke **40**(6): 2266-2267.

Dombeck, D. A., M. S. Graziano and D. W. Tank (2009). "Functional clustering of neurons in motor cortex determined by cellular resolution imaging in awake behaving mice." Journal of Neuroscience **29**(44): 13751-13760.

Dombeck, D. A., C. D. Harvey, L. Tian, L. L. Looger and D. W. Tank (2010). "Functional imaging of hippocampal place cells at cellular resolution during virtual navigation." Nature Neuroscience **13**(11): 1433-U1180.

Dombeck, D. A., A. N. Khabbaz, F. Collman, T. L. Adelman and D. W. Tank (2007). "Imaging large-scale neural activity with cellular resolution in awake, mobile mice." Neuron **56**(1): 43-57.

Dufour, S., Y. Atchia, R. Gad, D. Ringuette, I. Sigal and O. Levi (2013). "Evaluation of laser speckle contrast imaging as an intrinsic method to monitor blood brain barrier integrity." Biomedical Optics Express **4**(10): 1856-1875.

Duncan, D. D. and S. J. Kirkpatrick (2008). "Can laser speckle flowmetry be made a quantitative tool?" Journal of the Optical Society of America A **25**(8): 2088-2094.

Duncan, D. D. and S. J. Kirkpatrick (2008). Spatio-temporal algorithms for processing laser speckle imaging data. Biomedical Optics (BiOS) 2008, International Society for Optics and Photonics.

Dunn, A. K., T. Bolay, M. A. Moskowitz and D. A. Boas (2001). "Dynamic imaging of cerebral blood flow using laser speckle." Journal of Cerebral Blood Flow and Metabolism **21**(3): 195-201.

Engelbrecht, C. J., R. S. Johnston, E. J. Seibel and F. Helmchen (2008). "Ultra-compact fiber-optic two-photon microscope for functional fluorescence imaging in vivo." Optics Express **16**(8): 5556-5564.

Engelbrecht, C. J., F. Voigt and F. Helmchen (2010). "Miniaturized selective plane illumination microscopy for high-contrast in vivo fluorescence imaging." Optics Letters **35**(9): 1413-1415.

Falati, S., P. Gross, G. Merrill-Skoloff, B. C. Furie and B. Furie (2002). "Real-time in vivo imaging of platelets, tissue factor and fibrin during arterial thrombus formation in the mouse." Nature Medicine **8**(10): 1175-1181.

Faraday, N., K. Schunke, S. Saleem, J. Fu, B. Wang, J. Zhang, C. Morrell and S. Dore (2013). "Cathepsin G-dependent modulation of platelet thrombus formation in vivo by blood neutrophils." PLoS One **8**(8): e71447.

Fercher, A. F. and J. D. Briers (1981). "Flow Visualization by Means of Single-Exposure Speckle Photography." Optics Communications **37**(5): 326-330.

Ferezou, I., S. Bolea and C. C. Petersen (2006). "Visualizing the cortical representation of whisker touch: voltage-sensitive dye imaging in freely moving mice." Neuron **50**(4): 617-629.

Flusberg, B. A., J. C. Lung, E. D. Cocker, E. P. Anderson and M. J. Schnitzer (2005). "In vivo brain imaging using a portable 3.9 gram two-photon fluorescence microendoscope." Optics Letters **30**(17): 2272-2274.

Flusberg, B. A., A. Nimmerjahn, E. D. Cocker, E. A. Mukamel, R. P. Barretto, T. H. Ko, L. D. Burns, J. C. Jung and M. J. Schnitzer (2008). "High-speed, miniaturized fluorescence microscopy in freely moving mice." Nature Methods **5**(11): 935-938.

Ghosh, K. K., L. D. Burns, E. D. Cocker, A. Nimmerjahn, Y. Ziv, A. E. Gamal and M. J. Schnitzer (2011). "Miniaturized integration of a fluorescence microscope." Nature Methods **8**(10): 871-878.

Gobel, W., J. N. Kerr, A. Nimmerjahn and F. Helmchen (2004). "Miniaturized two-photon microscope based on a flexible coherent fiber bundle and a gradient-index lens objective." Optics Letters **29**(21): 2521-2523.

Greenberg, D. S. and J. N. Kerr (2009). "Automated correction of fast motion artifacts for two-photon imaging of awake animals." Journal of Neuroscience Methods **176**(1): 1-15.

Haruta, M., C. Kitsumoto, Y. Sunaga, H. Takehara, T. Noda, K. Sasagawa, T. Tokuda and J. Ohta (2014). "An implantable CMOS device for blood-flow imaging during experiments on freely moving rats." Japanese Journal of Applied Physics **53**(4).

Hecht, N., J. He, I. Kremenetskaia, M. Nieminen, P. Vajkoczy and J. Woitzik (2012). "Cerebral hemodynamic reserve and vascular remodeling in C57/BL6 mice are influenced by age." Stroke **43**(11): 3052-3062.

Heeger, D. J. and D. Ress (2002). "What does fMRI tell us about neuronal activity?" Nature Review in Neuroscience **3**(2): 142-151.

Helmchen, F., W. Denk and J. N. Kerr (2013). "Miniaturization of two-photon microscopy for imaging in freely moving animals." Cold Spring Harbor Protocols **2013**(10): 904-913.

Helmchen, F., M. S. Fee, D. W. Tank and W. Denk (2001). "A miniature head-mounted two-photon microscope. high-resolution brain imaging in freely moving animals." Neuron **31**(6): 903-912.

Hillman, E. M. (2007). "Optical brain imaging in vivo: techniques and applications from animal to man." Journal of Biomedical Optics **12**(5): 051402.

Hlatky, L., P. Hahnfeldt and J. Folkman (2002). "Clinical application of antiangiogenic therapy: Microvessel density, what it does and doesn't tell us." Journal of the National Cancer Institute **94**(12): 883-893.

Holtmaat, A., T. Bonhoeffer, D. K. Chow, J. Chuckowree, V. De Paola, S. B. Hofer, M. Hubener, T. Keck, G. Knott, W. C. A. Lee, R. Mostany, T. D. Mrsic-Flogel, E. Nedivi, C. Portera-Cailliau, K. Svoboda, J. T. Trachtenberg and L. Wilbrecht (2009). "Long-term, high-resolution imaging in the mouse neocortex through a chronic cranial window." Nature Protocols **4**(8): 1128-1144.

Holzer, M., C. Schmitz, Y. Pei, H. Graber, R.-A. Abdul, J. Barry, R. Muller and R. Barbour (2006). 4D functional imaging in the freely moving rat. Engineering in Medicine and Biology Society, 2006. EMBS'06. 28th Annual International Conference of the IEEE, IEEE.

Isshiki, M. and S. Okabe (2014). "Evaluation of cranial window types for in vivo two-photon imaging of brain microstructures." Microscopy (Oxf) **63**(1): 53-63.

Jones, P. B., H. K. Shin, D. A. Boas, B. T. Hyman, M. A. Moskowitz, C. Ayata and A. K. Dunn (2008). "Simultaneous multispectral reflectance imaging and laser speckle flowmetry of cerebral blood flow and oxygen metabolism in focal cerebral ischemia." Journal of Biomedical Optics **13**(4): 044007.

Kerr, J. N. and W. Denk (2008). "Imaging in vivo: watching the brain in action." Nature Review in Neuroscience **9**(3): 195-205.

Kerr, J. N. and A. Nimmerjahn (2012). "Functional imaging in freely moving animals." Current Opinion in Neurobiology **22**(1): 45-53.

Kirkpatrick, S. J., D. D. Duncan and E. M. Wells-Gray (2008). "Detrimental effects of speckle-pixel size matching in laser speckle contrast imaging." Optics Letters **33**(24): 2886-2888.

Kudo, C., A. Nozari, M. A. Moskowitz and C. Ayata (2008). "The impact of anesthetics and hyperoxia on cortical spreading depression." Experimental Neurology **212**(1): 201-206.

Ledochowitsch, P., E. Olivero, T. Blanche and M. M. Maharbiz (2011). A transparent μECoG array for simultaneous recording and optogenetic stimulation. Engineering in Medicine and Biology Society, EMBC, 2011 Annual International Conference of the IEEE, IEEE.

Li, N., J. E. Downey, A. Bar-Shir, A. A. Gilad, P. Walczak, H. Kim, S. E. Joel, J. J. Pekar, N. V. Thakor and G. Pelled (2011). "Optogenetic-guided cortical plasticity after nerve injury." Proceedings of the National Academy of Sciences of the United States of America **108**(21): 8838-8843.

Li, N., X. F. Jia, K. Murari, R. Parlapalli, A. Rege and N. V. Thakor (2009). "High spatiotemporal resolution imaging of the neurovascular response to electrical stimulation of rat peripheral trigeminal nerve as revealed by in vivo temporal laser speckle contrast." Journal of Neuroscience Methods **176**(2): 230-236.

Liu, Q., Y. Li, H. Lu and S. Tong (2014). "Real-time high resolution laser speckle imaging of cerebral vascular changes in a rodent photothrombosis model." Biomedical Optics Express **5**(5): 1483-1493.

Liu, R., Q. Huang, B. Li, C. Yin, C. Jiang, J. Wang, J. Lu, Q. Luo and P. Li (2013). "Extendable, miniaturized multi-modal optical imaging system: cortical hemodynamic observation in freely moving animals." Optics Express **21**(2): 1911-1924.

Mank, M., A. F. Santos, S. Direnberger, T. D. Mrsic-Flogel, S. B. Hofer, V. Stein, T. Hendel, D. F. Reiff, C. Levelt, A. Borst, T. Bonhoeffer, M. Hubener and O. Griesbeck (2008). "A genetically encoded calcium indicator for chronic in vivo two-photon imaging." Nauret Methods **5**(9): 805-811.

Masino, S. A., M. C. Kwon, Y. Dory and R. D. Frostig (1993). "Characterization of Functional-Organization within Rat Barrel Cortex Using Intrinsic Signal Optical Imaging through a Thinned Skull." Proceedings of the National Academy of Sciences of the United States of America **90**(21): 9998-10002.

McVea, D. A., M. H. Mohajerani and T. H. Murphy (2012). "Voltage-sensitive dye imaging reveals dynamic spatiotemporal properties of cortical activity after spontaneous muscle twitches in the newborn rat." Journal of Neuroscience **32**(32): 10982-10994.

Miao, P., H. Lu, Q. Liu, Y. Li and S. Tong (2011). "Laser speckle contrast imaging of cerebral blood flow in freely moving animals." Journal of Biomedical Optics **16**(9): 090502.

Mittmann, W., D. J. Wallace, U. Czubayko, J. T. Herb, A. T. Schaefer, L. L. Looger, W. Denk and J. N. Kerr (2011). "Two-photon calcium imaging of evoked activity from L5 somatosensory neurons in vivo." Nature Neuroscience **14**(8): 1089-1093.

Mozaffarian, D., E. J. Benjamin, A. S. Go, D. K. Arnett, M. J. Blaha, M. Cushman, S. de Ferranti, J.-P. Despres, H. J. Fullerton and V. J. Howard (2015). "Heart disease and stroke statistics-2015 update: a report from the american heart association." Circulation **131**(4): e29.

Murari, K., R. Etienne-Cummings, G. Cauwenberghs and N. Thakor (2010). An integrated imaging microscope for untethered cortical imaging in freely-moving animals. Engineering in medicine and biology society (EMBC), 2010 annual international conference of the IEEE, IEEE.

Murari, K., E. Greenwald, R. Etienne-Cummings, G. Cauwenberghs and N. Thakor (2009). Design and characterization of a miniaturized epi-illuminated microscope. Engineering in Medicine and Biology Society, EMBC, 2009 Annual International Conference of the IEEE, IEEE.

Murari, K., N. Li, A. Rege, X. Jia, A. All and N. Thakor (2007). "Contrast-enhanced imaging of cerebral vasculature with laser speckle." Appllied Optics **46**(22): 5340-5346.

Murari, K., N. Li, A. Rege, X. Jia, A. All and N. Thakor (2007). "Contrast-enhanced imaging of cerebral vasculature with laser speckle." Applied Optics **46**(22): 5340-5346.

Murayama, M., E. Perez-Garci, H. R. Luscher and M. E. Larkum (2007). "Fiberoptic system for recording dendritic calcium signals in layer 5 neocortical pyramidal cells in freely moving rats." Journal of Neurophysiology **98**(3): 1791-1805.

Murayama, M., E. Perez-Garci, T. Nevian, T. Bock, W. Senn and M. E. Larkum (2009). "Dendritic encoding of sensory stimuli controlled by deep cortical interneurons." Nature **457**(7233): 1137-1141.

Murray, C. J. and A. D. Lopez (2013). "Measuring the global burden of disease." New England Journal of Medicine **369**(5): 448-457.

Mutoh, H., A. Perron, W. Akemann, Y. Iwamoto and T. Knopfel (2011). "Optogenetic monitoring of membrane potentials." Experimental Physiology **96**(1): 13-18.

Nasrallah, I. and J. Dubroff (2013). "An overview of PET neuroimaging." Seminars in Nuclear Medicine **43**(6): 449-461.

Ng, D. C., H. Tamura, T. Mizuno, T. Tokuda, M. Nunoshita, Y. Ishikawa, S. Shiosaka and J. Ohta (2008). "An implantable and fully integrated complementary metal-oxide semiconductor device for in vivo neural imaging and electrical interfacing with the mouse hippocampus." Sensors and Actuators a-Physical **145**: 176-186.

Ng, D. C., T. Tokuda, S. Shiosaka, Y. Tano and J. Ohta (2008). "Implantable microimagers." Sensors **8**(5): 3183-3204.

O'Sullivan, T. D., R. T. Heitz, N. Parashurama, D. B. Barkin, B. A. Wooley, S. S. Gambhir, J. S. Harris and O. Levi (2013). "Real-time, continuous, fluorescence sensing in a freely-moving subject with an implanted hybrid VCSEL/CMOS biosensor." Biomedical Optics Express **4**(8): 1332-1341.

Obrenovitch, T. P., S. Chen and E. Farkas (2009). "Simultaneous, live imaging of cortical spreading depression and associated cerebral blood flow changes, by combining voltage-sensitive dye and laser speckle contrast methods." Neuroimage **45**(1): 68-74.

Osman, A., J. H. Park, D. Dickensheets, J. Platisa, E. Culurciello and V. A. Pieribone (2011). A head-mountable microscope for high-speed fluorescence brain imaging. Biomedical Circuits and Systems Conference (BioCAS), 2011 IEEE, IEEE.

Osman, A., J. H. Park, D. Dickensheets, J. Platisa, E. Culurciello and V. A. Pieribone (2012). "Design constraints for mobile, high-speed fluorescence brain imaging in awake animals." IEEE Transactions on Biomedical Circuits and Systems **6**(5): 446-453.

Park, J. H., J. Platisa, J. V. Verhagen, S. H. Gautam, A. Osman, D. Kim, V. A. Pieribone and E. Culurciello (2011). "Head-mountable high speed camera for optical neural recording." Journal of Neuroscience Methods **201**(2): 290-295.

Petersen, C. C., A. Grinvald and B. Sakmann (2003). "Spatiotemporal dynamics of sensory responses in layer 2/3 of rat barrel cortex measured in vivo by voltage-sensitive dye imaging combined with whole-cell voltage recordings and neuron reconstructions." Journal of Neuroscience **23**(4): 1298-1309.

Petty, G. W., R. D. Brown, Jr., J. P. Whisnant, J. D. Sicks, W. M. O'Fallon and D. O. Wiebers (1999). "Ischemic stroke subtypes: a population-based study of incidence and risk factors." Stroke **30**(12): 2513-2516.

Pham, C. T. (2006). "Neutrophil serine proteases: specific regulators of inflammation." Nature Review in Immunology **6**(7): 541-550.

Piyawattanametha, W., E. D. Cocker, L. D. Burns, R. P. J. Barretto, J. C. Jung, H. Ra, O. Solgaard and M. J. Schnitzer (2009). "In vivo brain imaging using a portable 2.9 g two-photon microscope based on a microelectromechanical systems scanning mirror." Optics Letters **34**(15): 2309-2311.

Rege, A., A. C. Seifert, D. Schlattman, Y. Ouyang, K. W. Li, L. Basaldella, H. Brem, B. M. Tyler and N. V. Thakor (2012). "Longitudinal in vivo monitoring of rodent glioma models through thinned skull using laser speckle contrast imaging." Journal of Biomedical Optics **17**(12): 126017-126017.

Rege, A., N. V. Thakor, K. Rhie and A. P. Pathak (2012). "In vivo laser speckle imaging reveals microvascular remodeling and hemodynamic changes during wound healing angiogenesis." Angiogenesis **15**(1): 87-98.

Rege, A., N. V Thakor and A. P Pathak (2012). "Optical imaging of microvascular morphology and perfusion." Current Angiogenesis **1**(3): 243-260.

Richards, L. M., E. L. Towle, D. J. Fox, Jr. and A. K. Dunn (2014). "Intraoperative laser speckle contrast imaging with retrospective motion correction for quantitative assessment of cerebral blood flow." Neurophotonics **1**(1): 015006.

Sambrano, G. R., W. Huang, T. Faruqi, S. Mahrus, C. Craik and S. R. Coughlin (2000). "Cathepsin G activates protease-activated receptor-4 in human platelets." Journal of Biological Chemistry **275**(10): 6819-6823.

Sato, Y., S. Nakajima, N. Shiraga, H. Atsumi, S. Yoshida, T. Koller, G. Gerig and R. Kikinis (1998). "Three-dimensional multi-scale line filter for segmentation and visualization of curvilinear structures in medical images." Medical Image Analysis **2**(2): 143-168.

Saunter, C. D., S. Semprini, C. Buckley, J. Mullins and J. M. Girkin (2012). "Micro-endoscope for in vivo widefield high spatial resolution fluorescent imaging." Biomedical Optics Express **3**(6): 1274-1278.

Sawinski, J., D. J. Wallace, D. S. Greenberg, S. Grossmann, W. Denk and J. N. Kerr (2009). "Visually evoked activity in cortical cells imaged in freely moving animals." Proc Proceedings of the National Academy of Sciences of the United States of America **106**(46): 19557-19562.

Schneider, C. A., W. S. Rasband and K. W. Eliceiri (2012). "NIH Image to ImageJ: 25 years of image analysis." Nature Methods **9**(7): 671-675.

Schrandt, C. J., S. M. Kazmi, T. A. Jones and A. K. Dunn (2015). "Chronic monitoring of vascular progression after ischemic stroke using multiexposure speckle imaging and two-photon fluorescence microscopy." Journal of Cerebral Blood Flow and Metabolism **35**(6): 933-942.

Schunke, K. J., T. K. Toung, J. Zhang, A. P. Pathak, J. D. Xu, J. Y. Zhang, R. C. Koehler and N. Faraday (2015). "A novel atherothrombotic model of ischemic stroke induced by injection of collagen into the cerebral vasculature." Journal of Neuroscience Methods **239**: 65-74.

Selak, M. A., M. Chignard and J. B. Smith (1988). "Cathepsin-G Is a Strong Platelet Agonist Released by Neutrophils." Biochemical Journal **251**(1): 293-299.

Senarathna, J., K. Murari, R. Etienne-Cummings and N. Thakor (2011). Design of a novel head-mountable microscope system for laser speckle imaging. Biomedical Circuits and Systems Conference (BioCAS), 2011 IEEE, IEEE.

Senarathna, J., K. Murari, R. Etienne-Cummings and N. V. Thakor (2012). "A miniaturized platform for laser speckle contrast imaging." IEEE Transactions on Biomedical Circuits and Systems **6**(5): 437-445.

Senarathna, J., A. Rege, N. Li and N. V. Thakor (2013). "Laser Speckle Contrast Imaging: theory, instrumentation and applications." IEEE Reviews in Biomedical Engineering **6**: 99-110.

Shaik, M., S. H. Kim, H. T. Zhao and E. M. Hillman (2015). Simultaneous Multi-Region Imaging Of Neuronal Activity, Hemodynamics And Speckle Flow In Awake Mice. Optics and the Brain, Optical Society of America.

Shao, B., M. G. Wahrenbrock, L. Yao, T. David, S. R. Coughlin, L. Xia, A. Varki and R. P. McEver (2011). "Carcinoma mucins trigger reciprocal activation of platelets and neutrophils in a murine model of Trousseau syndrome." Blood **118**(15): 4015-4023.

Sorg, B. S., M. E. Hardee, N. Agarwal, B. J. Moeller and M. W. Dewhirst (2008). "Spectral imaging facilitates visualization and measurements of unstable and abnormal microvascular oxygen transport in tumors." Journal of Biomedical Optics **13**(1): 014026.

Sorg, B. S., B. J. Moeller, O. Donovan, Y. Cao and M. W. Dewhirst (2005). "Hyperspectral imaging of hemoglobin saturation in tumor microvasculature and tumor hypoxia development." Journal of Biomedical Optics **10**(4): 44004.

Szuts, T. A., V. Fadeyev, S. Kachiguine, A. Sher, M. V. Grivich, M. Agrochao, P. Hottowy, W. Dabrowski, E. V. Lubenov, A. G. Siapas, N. Uchida, A. M. Litke and M. Meister (2011). "A wireless multi-channel neural amplifier for freely moving animals." Nature Neuroscience **14**(2): 263-269.

Tamaki, Y., M. Araie, K. Tomita, M. Nagahara, A. Tomidokoro and H. Fujii (1997). "Real-time measurement of human optic nerve head and choroid circulation, using the laser speckle phenomenon." Japanese Journal of Ophthalmology **41**(1): 49-54.

Theer, P., M. T. Hasan and W. Denk (2003). "Two-photon imaging to a depth of 1000 μm in living brains by use of a Ti: Al_2O_3 regenerative amplifier." Optics Letters **28**(12): 1022-1024.

Theuwissen, A. J. P. (2008). "CMOS image sensors: State-of-the-art." Solid-State Electronics **52**(9): 1401-1406.

Thevenaz, P., U. E. Ruttimann and M. Unser (1998). "A pyramid approach to subpixel registration based on intensity." IEEE Transactions on Image Processsing **7**(1): 27-41.

Trachtenberg, J. T., B. E. Chen, G. W. Knott, G. Feng, J. R. Sanes, E. Welker and K. Svoboda (2002). "Long-term in vivo imaging of experience-dependent synaptic plasticity in adult cortex." Nature **420**(6917): 788-794.

Ts'o, D. Y., R. D. Frostig, E. E. Lieke and A. Grinvald (1990). "Functional organization of primate visual cortex revealed by high resolution optical imaging." Science **249**(4967): 417-420.

Tye, K. M. and K. Deisseroth (2012). "Optogenetic investigation of neural circuits underlying brain disease in animal models." Nature Reviews Neuroscience **13**(4): 251-266.

Wang, L., S. L. Jacques and L. Zheng (1995). "MCML—Monte Carlo modeling of light transport in multi-layered tissues." Computer Methods and Programs in Biomedicine **47**(2): 131-146.

Warden, B. A., A. M. Willman and C. D. Williams (2012). "Antithrombotics for secondary prevention of noncardioembolic ischaemic stroke." Nature Reviews Neurology **8**(4): 223-235.

Weidner, N., J. P. Semple, W. R. Welch and J. Folkman (1991). "Tumor Angiogenesis and Metastasis - Correlation in Invasive Breast-Carcinoma." New England Journal of Medicine **324**(1): 1-8.

White, S. M., S. C. George and B. Choi (2011). "Automated computation of functional vascular density using laser speckle imaging in a rodent window chamber model." Microvascular Research **82**(1): 92-95.

Yang, G., F. Pan, C. N. Parkhurst, J. Grutzendler and W. B. Gan (2010). "Thinned-skull cranial window technique for long-term imaging of the cortex in live mice." Nature Protocols **5**(2): 201-208.

Yuan, S., A. Devor, D. A. Boas and A. K. Dunn (2005). "Determination of optimal exposure time for imaging of blood flow changes with laser speckle contrast imaging." Applied Optics **44**(10): 1823-1830.

Zhang, J., R. E. Campbell, A. Y. Ting and R. Y. Tsien (2002). "Creating new fluorescent probes for cell biology." Nature Reviews Molecular Cell Biology **3**(12): 906-918.

Zinkstok, S. M., Y. B. Roos and A. investigators (2012). "Early administration of aspirin in patients treated with alteplase for acute ischaemic stroke: a randomised controlled trial." Lancet **380**(9843): 731-737.

Zivin, J. A. (2009). "Acute Stroke Therapy With Tissue Plasminogen Activator (tPA) Since It Was Approved by the US Food and Drug Administration (FDA)." Annals of Neurology **66**(1): 6-10.

CURRICULUM VITAE

Hang Yu

Email: hangyu.jhu@gmail.com

EDUCATION

Johns Hopkins University, Baltimore, MD, USA (GPA 3.96/4.0**)**

M.S. in Biomedical Engineering, 2015 (expected)

Dissertation: *Multi-modal optical neuroimaging and applications*

Zhejiang University, Hangzhou, Zhejiang, China (GPA 3.83/4.0)

B.S. in Optical Engineering, 2013

PUBLICATIONS

- **Yu, H.**, Senarathna, J., Tyler, B. M., Thakor, N. V., & Pathak, A. P. (2015). Miniaturized optical neuroimaging in unrestrained animals. *NeuroImage*, *113*, 397-406.
- Miao, P., Chao, Z., Feng, S., **Yu, H.**, Ji, Y., Li, N., & Thakor, N. V. (2015). Local scattering property scales flow speed estimation in laser speckle contrast imaging. *Laser Physics Letters*, *12*(7), 075601.
- Wang, C., Ding, Z., Mei, S., **Yu, H.**, Hong, W., Yan, Y., & Shen, W. (2012). Ultralong-range phase imaging with orthogonal dispersive spectral-domain optical coherence tomography. *Optics letters*, *37*(21), 4555-4557.

SELECTED PROJECTS

Graduate research assistant, Johns Hopkins University (2013-2015)

- Design and development of a miniaturized multi-modal microscope for imaging in awake, freely moving animals.
- Effects of cranial window type on monitoring neurovasculature using laser speckle contrast imaging.

Undergraduate researcher, University of Houston (2012)

- Optical fiber thermometer based on blackbody radiation cavity.

Research assistant, Zhejiang University (2010-2012)

- Ultrasensitive microfiber absorption detection in a microfluidic chip.